GEOLOGICAL SURVEY OF CANADA
OPEN FILE 7063

Magnetotelluric soundings in the Committee Bay Belt, northern Churchill area, Nunavut

J.E. Spratt, D.B. Snyder, and J.A. Craven

2012

GEOLOGICAL SURVEY OF CANADA
OPEN FILE 7063

Magnetotelluric soundings in the Committee Bay Belt, northern Churchill area, Nunavut

J.E. Spratt[1], D.B. Snyder[2], and J.A. Craven[2]

[1] Magnetotelluric Consultant, Wakefield, Quebec J0X 3G0
[2] Geological Survey of Canada, 615 Booth Street, Ottawa, Ontario K1A 0E9

2012

This publication is available from the Geological Survey of Canada Bookstore
(http://gsc.nrcan.gc.ca/bookstore_e.php).
It can also be downloaded free of charge from GeoPub (http://geopub.nrcan.gc.ca/).

Publications in this series have not been edited; they are released as submitted by the author.

Table of Contents

Introduction

As part of Natural Resource Canada's GEM (Geo-mapping for energy and minerals) program, the Diamonds project is designed to map the deep lithosphere beneath key parts of the Northwest Territories and Nunavut of northern Canada. The primary goal of this project is to further our understanding of the potential for diamonds and reduce the risk in their exploration. To aid in obtaining this goal, it has been proposed to acquire long-period and broadband magnetotelluric (MT) data along five separate corridors throughout Nunavut and the Northwest Territories during the 2010, 2011, and 2012 field seasons. During the summer of 2010, MT data were collected along a 300 km-long transect, the Diamonds I MT corridor, that extends from southwest of Repulse Bay to the south end of the Boothia Peninsula, through a portion of the Rae craton in the Churchill Province of the eastern Canadian Shield (Spratt et al, 2011). During the summer of 2011 MT data were collected along the northern and northwestern half of two profiles extending north and northwest of Wager Bay, as well as at several isolated locations throughout the region designed to fill gaps in future 3-D models. These data will enhance and complement interpretations of previous MT data collected throughout eastern Nunavut, with the long term goal of generating a regional 3-dimensional model of the conductivity structure of the lithosphere (Figure 1). The 2011 MT data have been processed using modern, robust, remote-referencing methods and have been analyzed for dimensionality, effects of distortion, geo-electric strike angles, and penetration depths. Preliminary 2-D models have been derived along four separate profiles.

Data Acquisition and processing

Prior to the 2011 field operations, the MT equipment were tested, and packed for shipment to Rankin Inlet, Nunavut. The field campaign took place during the month of August and was based out of North Country Gold Corporation's Hayes River camp, located ~100 km northwest of Wager Bay. The data have been divided into four separate profiles for analysis and 2-D modelling. Broadband (BBMT) and long period (LMT) MT data were acquired at a total of 31 site locations, nine of which were located along the westernmost 140 km-long northwest-to-southeast profile (line 1), eight were located along a 110 km-long north-south profile (line 2), five sites were located along the easternmost 90 km-long northwest to southeast profile (line 3) and the remaining sites were distributed throughout the study area either as infill along the northern section of the 2010 profile (line 4) or regionally for future 3D modelling (Figure 2).

Long period (LMT) data were collected at ten of the site locations using NiMS recording instruments; data acquisition durations and locations for each site are

shown in table 1. The electrical fields were recorded in the two horizontal, perpendicular directions using lead-lead-chloride porous pot electrodes and the magnetic fields were recorded in the two horizontal, plus the vertical direction using a 3-component fluxgate magnetometer. Data were collected for a minimum of 8 days continuously with two exceptions. At site dmn104, the site was damaged by animal activity after 1.8 days of acquisition and it was determined that relocating the long period site was necessary. At site dmn116, the battery failed after 2 days of acquisition, likely a result of old batteries and cold weather. The data from each site were converted from the recorded binary format to ascii format using John Booker's conversion code and were then processed using the multi-remote-reference, robust, cascade decimation code of Jones (Jones and Jödicke, 1984). Apparent resistivity and phase response curves as a function of period were generated for each of the LMT sites in the north-south (XY) and east-west (YX) directions. In general the data quality is good with smooth response curves and low error bars in the period range of 10 s up to 10,000 s (Figure 3a).

Broadband (BBMT) data were collected at a total of 29 site locations, including the 10 long period locations using a combination of MTU-5 and MTU-5a Phoenix Geophysics recording instruments and sensors. The two horizontal perpendicular magnetic fields were recorded using two separate MTC50 Phoenix coils, and the vertical fields were recorded using either a MTC30 or a MTC80 Phoenix coil. Data were collected for at minimum of 17 hours up to a maximum of 3 days (Table 1). The BBMT data were processed from time series to response functions using robust remote reference techniques (Method 6 in Jones et al., 1989), as implemented by the Phoenix Geophysics software package MT2000, and yielded high quality apparent resistivity and phase response curves in the period range of 0.004 –1,000 s for most sites (Figure 3b). At sites where both LMT and BBMT data were collected at the same location, the response curves were merged together to generate one file with a period range of 0.004 –10,000 s, spanning nearly 8 decades (Figure 3d). An issue with the software and method of programming the two different recording box types (MTU-5 and MTU-5a) resulted in a filter setting error during the acquisition of six broadband sites (dmn106, dmn107, dmn109, dmn114, dmn117, and dmn119). Data were recorded at one neaby location (site dmn113) using both instrument types at different times allowing for the comparison of the resulting response curves. This comparison showed that aside from a major static shift of the apparent resistivity curves, the data were reliable at periods longer than 0.08s (Figure 3c). Static shift corrections determined from the apparent resistivity values at the long period data and neighboring broadband sites were applied to each of the affected sites.

Data analysis

Decomposition Analysis

Groom-Bailey decomposition analysis was undertaken in order to understand the degree of dimensionality, determine the most appropriate geo-electric strike direction (where the data are 2-dimensional), and ascertain and remove the effects of galvanic distortion in the data (Groom and Bailey, 1989). Single site decompositions were applied to each of the 2011 MT sites using the method described in McNeice and Jones (2001). At frequencies where the phase difference between the TE- and TM-modes is minimal (<10°) the data can be considered 1-dimensional (1-D), or independent of the geo-electrical strike angle. Where the phase difference is larger, the data are more dependent on direction and 2-D models need to be inverted at the appropriate geo-electric strike angle in order to accurately represent the subsurface conductivity structure beneath a profile. Ideally a model can be generated along a profile at one strike angle for all periods. Wherever the subsurface structure is complex and this angle varies along profile or with depth, the profile may need to be divided into sections and modelled separately at the different geo-electric strike angles.

The strike directions resulting from single-site, single-decade-period-band decompositions (noting the 90° ambiguity inherent in this analysis), with an error floor set to 3.5% (equivalent to 2° phase), are shown in figure 4. At periods below 0.01 s most of the sites show low phase differences with few exceptions, suggesting that locally and at shallow depths the data are predominantly 1-D. The results of strike analysis are discussed for each of the 4 lines separately: line 1 - the westernmost northwest-to-southeast profile, line 2 - the 2011 north-south profile, line 3 - the easternmost northeast-to-southwest profile, and line 4 - the northern half of the 2010 profile (including the sites collected in 2010 and 2011).

Strike analysis along line 1 reveals clear along-profile differences, where the southern half of the profile appears to be predominantly 1-D at periods longer than 1 s (Figure 4). The northern half of the profile indicates preferred strikes angles of 33°– 47° at periods between 0.1 and 10 s. At longer periods all of the data show low phase differences (< 10°) with the exception of a few sites at very long periods (>100 s) showing angles of 70°–77°.

Plots of phase differences and strike directions along line 2, indicate low phase differences (<10°) for most of the sites at most of the periods, suggesting that the data are predominantly 1-D. The southernmost few sites show a weak preference for a strike of ~75° at periods between 0.1–1 s, a strike of ~45° at periods between 1 and 100 s, and a strike of ~79° at periods greater than 100 s.

Strike analysis of the sites along line 3 reveal large phase differences at periods

greater that 1 s, however the strike directions are largely inconsistent ranging between 20° and 79° at most periods. This is a strong indication of 3-dimensionality in the data, and a 2-D model may not accurately represent the subsurface structure.

Along line 4, maximum phase differences are observed between 0.1 and 1000 s (Figure 4). At periods below 0.1 s there is a large degree of scatter in the strike direction, sites that show a larger phase split (dmn013, dmn025, and dmn029) have a preferred strike direction of 57–61°, consistent with the regional geologic trend, however the strong changes in phase differences and the scatter of strike angles suggests that localized structures are influencing the data. Analysis of the 2010 data revealed that several of these sites showed strong distortion at the shortest periods, likely resulting from the presence of clays that blanket a large portion of the region. At periods between 0.1 and 1 s, phase differences are moderate ($< 20°$) with a preferred strike angle of 70°-73° for the northernmost sites and 22°-27° for the southernmost sites. At periods between 1–10 s, all of the sites along the profile (with the exception of sites dmn113 and dmn027 that are located off-line) the data show a consistent preference for a strike angle of 21°–24° (Figure 4c). At longer periods (> 10 s) there is a distinct change with a preferred strike angle of 75°–77° for the northernmost sites and angle of 50°-60° for the southern most sites.

Because the depth of penetration is dependent on the period and resistivity of the subsurface, the depth at a particular period may be different from one site to the next. In general basic depth estimates show that periods below 10 s roughly correspond to crustal depths (< 40 km) and periods greater than 10 s are likely penetrating into the upper mantle (>40 km). The short period distortion, anomalous strike angles in the sites that are off-profile, and the distribution of the station locations make this region ideal for generating a localized 3-D model.

The regional geology (Figure 2), aeromagnetic geometry (Figure 5), and bouguer gravity anomalies (Figure 6) show a regional northeast-to-southwest trend, indicating the TE-mode direction (component of MT data that corresponds to the geologic along-strike direction), with the TM-mode perpendicular to strike. At the longest periods there is a consistent preference of 70°–77°, roughly parallel to the plate motion vector and thus probably representing the TE-mode (Figure 5).

The misfit values from the Groom-Bailey decomposition analysis for each site have been plotted against increasing periods for 3 different strike angles along each of the profiles (Figures 7, 8, 9, and 10). A misfit value of < 2 indicates that a 2-D model of the earth at that strike angle could be adequately represented by the data, a misfit value that is greater than 2 regardless of geo-electric strike angle suggests that 2-D distortion effects cannot be resolved and indicates the need for 3-dimensional modelling.

Along line 1, the data were decomposed at strike angles of 35°, 45°, and 75°

(Figure 7). The geo-electric strike angle that best fits most of the sites over most of the period ranges is 45°. Three sites appear to be strongly influenced by the strike angle selection, sites DMN107, DMN103, and DMN102, particularly at longer periods. Several of the sites show high misfit values at all strike angles at the shortest periods (marked by black ellipses in figure 7), indicating localized 3-D distortion effects. These periods have been removed from the data set prior to initiating 2-D inversions. Two-dimensional models have been generated with the data recalculated at a strike angle of 45 degrees.

Along line 2, the data were decomposed at a strike angle of 35°, 45°, and 75° (Figure 8). Here the northern half of the profile appears to be predominantly 1-d, where the misfit values are independent of the strike angle. Consistent with the plots of the preferred strike angles at decade period bands (Figure 4), the southern half of the profile shows a preference for a strike angle of 75° at periods below ~1 s and a strike angle of 45° at periods greater than ~10 s particularly at sites DMN118 and DMN119. Two-dimensional models have been generated with the data recalculated at a strike angle of 45° and 75° in order assess features in the models that may be affected by a change in strike angle.

Along line 3, the data were decomposed at a strike angle of 24°, 63°, and 79° (Figure 9). Overall the geo-electric strike angle that best fits most of the data over most of the period range is 79°, however two of the five sites (sites DMN021 and DMN022) still show misfits up to a value of 3. Two-dimensional models have been generated with the data recalculated at a strike angle of 79°, but results of regional 3-D modelling will likely be more accurate.

Along line 4, the northern half of the 2010 profile, the data were decomposed at strike angle of 24°, 57°, and 75° (Figure 10). The northwestern most 2 sites and the long periods at site DMN015, DMN026, and DMN027 show a preference for a strike of 70°, whereas at periods below 1 sites DMN028, DMN026, DMN016, DMN027 and DMN029 show a preference for a strike of 24°. Two-dimensional models have been generated with the data recalculated at strike angles of 24° and 75°. In general, the central part of this line show a strong degree of scatter in the preferred geo-electric strike angle and at the lowest periods sites DMN027 and DMN029 have misfits above 3 regardless of the angle. The site locations in this region do not all fall along a 2-D profile but are distributed over an area of roughly 60 sq km, making this region ideal for a localized 3-D model.

Depth estimates

Penetration depths of each mode (TM and TE) beneath each site were roughly estimated using Schmucker's c-function analysis, which calculates the depth of maximum eddy current flow (Schmucker, 1970). These estimates indicate that the

data at most of the sites penetrate to > 200 km depths in at least 1 mode, and in some cases to > 350 km (Figure 11), these depths are sufficient to image the deep lithosphere of the Earth beneath the profile. Line 4 is an exception as only 2 of the 5 sites along line 4 show deep penetration. It is unlikely that the deep lithosphere can be imaged along this profile, however, the 2 deep penetrating sites will aid in resolving the deep structure of regional 3-D models.

Ocean effects

The presence of sea water can have significant effects on MT data, due to the sharp contrast in resistivity between the land and the ocean (Schmucker, 1970; Menveillie et al., 1982). The coastal effects are typically observed in the long period data and the severity of these effects is dependent on the salinity of the sea water, the conductivity structure of the subsurface, the depth of the ocean, and the proximity of the MT site to the coast (e.g., Jones, 1981; Santos et al., 2001; Pous et al., 2003). In order to assess the coastal effects on this data set, a 3-D mesh was created with ocean resistivity values of 0.3 ohm-m extending to depths between 50 and 500 m, (approximated from the International Bathymetric Chart of the Arctic Ocean : http://www.ngdc.noaa.gov/mgg/bathymetry/arctic/arctic.html), and a uniform land resistivity values of 1000 ohm-m (Figure 12a). A forward inversion then calculates synthetic response curves at the recorded site locations. This method of determining coastal effects is a rough guide as the coast line is not exact, the depth and resistivity of the ocean water is approximated, and a uniformly resistive earth was used rather than a layered or structured earth. It is therefore only used to illustrate caution in interpreting 2-dimensional models that include long period data near the coast.

The calculated response curves indicate that there may be some effect in the northernmost sites along line 4, particularly at site DMN013 at periods longer than 10s (Figure 12a), however sites further to the west are largely unaffected. As the ocean depths are shallow in the northwest region of the survey area, there little to no effects are observed at the site locations along lines 2 and 3 (Figure 12b). The strongest effect is noted at sites along the westernmost profile (line 3), at a periods as short as 1 s (Figures 12c). Depth analysis, similar to that described above, for site DMN013 shows that 10 s corresponds to a depth of ~ 20 km, suggesting that a conductivity model of lithosphere using 2-D methods, may be severely distorted by ocean effects. This site has not been included in the 2-D models generated along line 4. Ocean effect and depth investigations of the 2010 data indicated that the remaining sites along line 4 were largely unaffected by sea water and could be used to generate 2-D models of the deep lithosphere (Spratt et al, 2011). Depth analysis of site DMN023 shows that a period of 1 s in the YX mode (the recorded east-west

direction) corresponds to depths of < 20 km, and site DMN022 to depths of ~ 40 km. This indicates that crustal features may be resolved along line 3, but 2-D modelling of the deep lithosphere may be unreliable.

Data Modeling

The distortion-corrected, regional 2-D responses from sites along the 4 lines described above have been imported into the WinGlink MT interpretation software package. Each site has been manually edited to remove data points with large error bars or large scatter. Additionally data that were shown to have high misfit values, primarily data in the shortest period range, in the decomposition analysis were removed. Where one apparent resistivity curve of one mode was much higher than another, the curve was dropped to match that of the other curve at the shortest period. This helps to reduce the effect of anisotropic shift, but does not account for the static shift cases were both curves are affected.

1-D Models
One-dimensional layered earth models were generated for each site using Occam's inversion codes as implemented by the WinGlink MT interpretation software package and were stitched together to form cross-sections along the 4 lines (Figures 13a, 14a, 15a, and 16a). Pseudosections of the phase responses for each of the sites along the profile were generated for both the TE- and TM-modes (Figures 13b, 14b, 15b, and 16b). As previously described in the phase difference plots, where these sections are similar, the 1-D models can be considered to be a valid representation of the Earth. The dashed red boxes indicate the areas where the data are predominantly 1-D and the stitched 1-D models show a laterally uniform layered Earth. The data outside the red box, show much more complex structure requiring 2-D, or 3-D modelling. Along line 1, the westernmost profile, the data can be regarded as 1-D only for the shortest frequencies, to depths of approximately 10 km (Figure 13). Along line 2, the northern half of the profile in both the stitched 1-D models and pseudosections appears to be 1-D to periods of nearly 1000 s, depths of ~ 80 - 100 km, whereas the southern half of the profile is 2-D even at short periods (Figure 14). The 1-D models and phase pseudosections along line 3, the easternmost profile, show the data to be predominantly 2-D over the entire period range (Figure 15). Consistent with the results from 2010, the 1-D models and phase pseudosections along line 4 show the data to be predominantly 2-D with the exception of the southern most two sites, where the data are 1-D to periods of ~1 s, equivalent to depths of ~ 30 km (Figure 16).

2-D models

Two-dimensional models of the distortion corrected responses calculated at the most appropriate geo-electric strike direction were generated for each of the profiles using the WinGlinkTM interpretation software package that implements Rodi and Mackies (2001) inversion algorithm . The 2-D inversion code searches iteratively for the smoothest model that best fits the data by attempting to trade off the fit to the observed data (data misfit) with the squared Laplacian (smoothing term) of the horizontal and vertical resistivity gradients. The inversion program searches for the smoothest, best-fit model with the least deviation from the starting model, which is usually a half space (Mackie and Madden, 1993). This means that the models found represent the minimum structure required to fit the data with an acceptable misfit.

In order to determine the most appropriate smoothing value to use, several models were generated from the data using the entire period range of 0.004 –10,000 s of both the TM- and TE-modes along each of the 4 lines. The error floor were set to 30% for the apparent resistivity to account for static shift effects, and 7% for the phase. For each model the smoothness parameter, tau, was changed after 100 iterations in order to determine the most appropriate tau value for the data set. Figure 17 illustrates the trade-off between the roughness of the model, defined by the tau parameter, and the fit of the model to the data, RMS, along lines 1, 2, and 3. These plot indicate that a tau value of 5-6 would result in the smoothest model with the best fit to the data along line 1, a value of 6–10 would be appropriate along lines 2 and 3. Results from the 2011 analysis showed that a value of 7 would result in the smoothest model with the best fit to the data along line 4 (Spratt et al., 2011).

In an attempt to determine the most appropriate parameters for this data set, several models were generated using different data components and parameters at each of the different strike angles along lines 1, 2, and 3. Models shown include data from the TE- and TM-modes, the inversions were initiated with a homogeneous half space of 500 ohm-m, and the phases were set with a 2° error floor. Initially the apparent resistivities were set with an error floor of 7%, and subsequently with an error floor of 30% to account for static shift effects. Results after 100 iterations showed similar conductivity structure, suggesting that static shift effects are minimal. Models were generated along line 1 using data recalculated at strike angle 45°, with a mesh consisting of 73 rows and 123 columns. Inversions were executed along line 2 with a mesh consisting of 76 rows and 106 columns, using data recalculated at a strike angle of 45° and 75° in order to asses which features are affected by the change in assigned geo-electric strike angle. A mesh of 68 rows and 83 columns was used for line 3, with data recalculated at 79°.

Analysis from 2010 determined that a strike angle of 55° resulted in the lowest

RMS value, implying that this angle was the most appropriate for representing the whole 2010 profile, but that differences between the models at different strike angles were observed predominantly at the northwestern most extent of the profile, in the vicinity of line 4. It was suggested that inverting data along the northern half of the profile alone using the short period data at the appropriate 24° strike angle and the long period data at 70° (or 75° from the new 2011 strike analysis) would result in a model that better represents the local structure beneath the profile. A mesh of 72 rows and 121 columns was used for each model.

Preliminary 2-D models for Lines 1–4

Line 1

Preliminary two-dimensional models of the MT data along line 1 reveal conductivity structure of the crust and mantle lithosphere (Figure 18). The crust is imaged as a resistive layer (>10 000 ohm-m) extending to depths of 30 - 34 km. The southeastern half of the model indicates that the resistive crust is underlain by a less resistive layer (~2000 ohm-m), further modelling is needed to assess whether this layer lies in the lower crust or uppermost mantle. This less resistive layer is not laterally continuous beneath the 3 northernmost sites, and an anomalous a mid-to-lower crustal conductor (<100 ohm-m) is imaged beneath site DMN104. This change from northwest to southeast beneath site DMN104 is consistent with changes observed in the strike analysis. At depths between 50–150 km, the southeastern half of the model shows a resistive upper mantle (~8000 ohm-m), however further to the northwest, there appears to a southeast dipping structure with resistivities values of ~1000 ohm-m. At depths ranging from 150 km beneath the southeastern end of the profile, to 225 km beneath the northwestern end of the profile, there is an decrease in resistivity to ~400 ohm-m. This may represent the boundary between the lithosphere and the underlying asthenosphere.

Line 2

Two separate models have been generate along line 2, one at a strike of 45° (Figure 19a) and one at a strike of 75° (Figure 19b). At depths up to 100 km the models are very similar showing a resistive layer, likely Archean orthogneiss in the crust, that ranges in thickness from 15 to 25 km along the profile. This resistive material is underlain by a less resistive lower crustal layer (~1000 ohm-m) that, although varying in depth and thickness, is present along the entire length of the profile. Similar to line 1, a mid-to-lower crustal conductor (< 100 ohm-m) is imaged beneath site DMN111 that lies along strike from that found beneath DMN104. Both of these locations (along lines 1 and 2) correlated with a change in the regional bouguer gravity signature (Figure 6) and may represent structure that

separates granulite facies orthogneiss from lower grade Archean crust. The deeper structure along line 2 varies significantly between the two models. Strike analysis suggests that the models generated at a geo-electric strike angle of 45° will better resolve the deep structure, particularly beneath the southern end of the profile (Figure 19a). This model shows an decrease in resistivity ranging between 180–200 km, likely the lithosphere-asthenosphere boundary.

Line 3

The preliminary models derived along line 3 shows marked differences in comparison to the other lines (Figure 20). In general, the structure in the crust appears to be much more complex with resistivity values ranging from 500 –10 000 ohm-m, dropping to < 10 ohm-m in isolated locations. The base of the crust cannot be defined and there does not appear to be a moderately resistive layer in the crust and/or upper mantle as observed along the other lines. The mantle lithosphere is imaged as very resistive with values >10,000 ohm-m. The central part of the profile, beneath the two sites that showed sufficient penetration depths (dmn021 and dmn022, figure 11), there appears to be a slight decrease in resistivity at depths of ~225 km. The lower resistivity values, however, are still much higher than those observed at asthenospheric depths along the other lines. As previously discussed, the data along this line are likely largely distorted, a result of 3-dimensionality and ocean sea water effects, and 2-D models may not represent an accurate image of the subsurface conductivity structure.

Line 4

Preliminary models along line 4 show major differences in both the crust and upper mantle between the inversions at a strike of 24° (Figure 21a) and at a strike of 75° (Figure 21b). The misfit value for results at 75° (RMS of 3.8) is much higher than that for 24° (RMS of 2.1) suggesting that the latter is a more reliable model for the whole profile. These strong differences, however, highlight the need for a localized 3-D model of the region, particularly in the vicinity of the diamond-bearing kimberlite field (between sites DMN017 and DMN014). At a strike of 24° the general conductivity structure is similar to that along the other 3 lines, with a resistive crust underlain my a less resistive lower crust and/or uppermost mantle. The lithospheric mantle shows resistivity values of ~8000 ohm-m, with a decrease in resistivity beneath the central portion of the profile. A decrease in resistivity at depths of 200 –225 km may represent a change from resistive mantle lithosphere to a more conductive asthenosphere. The significant changes in the lateral structure of both the crust and lithospheric mantle are observed beneath the kimberlite field and may be related to diamond formation and emplacement.

Conclusions

Careful processing and analysis of the 2011 Diamonds MT data collected have provided a good understanding of dimensionality, and distortion of the data and show that the quality of the data is sufficient to model the lithospheric conductivity structure. Decomposition analysis shows that the geo-electric strike angle varies across the region, and in some areas with depth. Modeling of the data at different strike angles using different variables has helped to determine some of the inversion parameters that should be used to provide an accurate image of the subsurface. Preliminary 1-D and 2-D models reveal some structure that appears to be consistent in the data. These models also illustrate the need for additional 2-D and 3-D inversions required to further resolve the subsurface conductivity structure. In general a resistive crust in underlain by a less resistive lower crust and/or upper mantle. Some structure is noted in the mantle lithosphere and a decrease in resistivity between 150–225 km likely marks the lithosphere –asthenosphere boundary. Hypothesis testing should be undertaken to assess the sensitivity of the data to various features, particularly the deep structure beneath the profiles.

References

Groom, R.W., and R.C. Bailey, 1989: Decomposition of magnetotelluric impedance tensors in the presence of local three-dimensional galvanic distortion; Journal of Geophysical Research, v. 94, p. 1913 –1935.

A.G. Jones, 1981: Geomagnetic Induction Studies in Scandinavia - II. Geomagnetic Depth Sounding, Induction Vectors and Coast-Effect; Journal of Geophysics, v.50, p. 23 –36.

Jones, A.G., Chave, A.D., Auld, D., Bahr, K. and Egbert, G., 1989: A comparison of techniques for magnetotelluric response function estimation; Journal of Geophysical Research, v. 94, p. 14,201 –14,213.

Jones, A.G., and H. Jodicke, 1984: Magnetotelluric transfer function estimation improvement by a coherence-based rejection technique, paper presented at the 54th Society of Exploration Geophysics Annual General Meeting, Atlanta, George, 2-6 December, Abstract volume, pp. 51-55.

Jones, A.G., and J.E. Spratt, 2001: A simple method for deriving the uniform field MT responses in auroral zones; Earth and Planetary Science Letters, v. 54, p. 443–450.

Jones, A.G., A.D. Chave, G.D. Egbert, D. Auld, and K. Barh, 1989: A comparison of techniques for magnetotelluric response function estimation; Journal of Geophysical Research, v. 94, p. 14210–14213.

Mackie, R.L., and T.R. Madden, 1993: Three-dimensional magnetotelluric inversion using conjugate gradients; Geophysical Journal International, V. 115, p. 215–229.

McNeice, G.W., and A.G. Jones, 2001: Multisite, multifrequency tensor decomposition of magnetotelluric data; Geophysics, v. 66, p. 158 –173.

Menvielle, M.J.C., P. Rossignal, and P. Tarits, 1982: The coast effect in terms of deviated electric currents: A numerical study; Physics of the Earth and Planetary Interiors, v. 28, p. 118–128.

Pous, J., W. Heise, P.A. Schegg, G. Munoz, J. Mart, and C. Soriano, 2002. Magnetotelluric study of the Las Canadas caldera (Tenerife, Canary Islands): structural and hydrogeological implications; Earth and Planetary Science Letters, v. 204, p. 249–263.

Santos, F. A. M., M. Nolasco, E. P. Almeida, J.Pous and L.A. Mendes-Victor: 2001. Coast effects on magnetic and magnetotelluric transfer functions and their correction: application to MT soundings carried out in SW Iberia; Earth and Planetary Science Letters, v.186, p. 283–295.

Schmucker, U., 1970. Anomalies of geomagnetic variations in the southwestern United States, Bull. Scripps Ints. Oceanogr. v. 13, 165 p.

Skulski, T., Paul, D., Buckle, J., Sandeman, H., Berman, R., Pehresson, S., Rainbird, R., Davis, W., Kerswill, J., and Sandborn-Barrie, M., in prep. Bedrock geology and regional synthesis of the north-central Rae domain, western Churchill Province, Nunavut, Canada; Geological Survey of Canada, Open File 5577, 1:5500000 scale.

Spratt, J.E., Snyder, D.B. and Craven, J.A., 2011. A magnetotelluric survey across the Committee Bay belt and Rae craton in the Churchill province of Nunavut; Geological Survey of Canada, Open File 6825, 28 p.

Table 1. Site type, location, and recording times for each of the MT sites collected along during the 2011 Diamonds MT field season.

Site Name	Data Range	Latitude	Longitude	Duration of acquisition
dmn101	LMT	67.0790	-94.5640	18.3 days
dmn104	LMT	66.7509	-93.7412	1.8 days
dmn107	LMT	66.4035	-93.1173	8.6 days
dmn110	LMT	67.2023	-91.5623	8 days
dmn113	LMT	66.6616	-91.5570	16 days
dmn115	LMT	66.2493	-91.4356	15.9 days
dmn116	LMT	67.2817	-92.9363	1.8 days
dmn013	LMT	68.1312	-90.0818	12.2 days
dmn018	LMT	66.8650	-87.4019	11.1 days
dmn019	LMT	67.0843	-86.1212	13.9 days
dmn013	BBMT	68.1312	-90.0818	18.3 hours
dmn020	BBMT	66.9586	-85.7882	17.3 hours
dmn021	BBMT	66.8086	-85.4026	16.7 hours
dmn022	BBMT	66.6773	-85.0545	20 hours
dmn023	BBMT	66.5579	-84.6922	19.4 hours
dmn026	BBMT	68.2719	-90.9071	45.6 hours
dmn027	BBMT	68.2056	-90.5010	45.3 hours
dmn028	BBMT	68.1963	-91.1781	83.6 hours
dmn029	BBMT	68.0210	-90.9321	70.2 hours
dmn101	BBMT	67.0790	-94.5640	44.7 hours
dmn102	BBMT	66.9648	-94.3565	44.5 hours
dmn103	BBMT	66.8260	-94.0524	43.8 hours
dmn104	BBMT	66.7509	-93.7412	42 hours
dmn105	BBMT	66.6232	-93.5855	21.5 hours
dmn106	BBMT	66.5096	-93.3413	44 hours
dmn107	BBMT	66.4035	-93.1173	45.2 hours
dmn108	BBMT	66.2859	-92.9955	57.8 hours
dmn109	BBMT	66.1398	-92.8089	63.7 hours
dmn110	BBMT	67.2023	-91.5623	43.2 hours
dmn111	BBMT	67.0718	-91.5893	63.7 hours
dmn112	BBMT	66.8446	-91.5110	35 hours
dmn113	BBMT	68.1312	-90.0818	42.7 hours
dmn114	BBMT	66.4620	-91.4740	41.9 hours
dmn115	BBMT	66.2493	-91.4356	36.1 hours
dmn116	BBMT	67.2816	-92.9363	43.1 hours
dmn117	BBMT	66.6195	-90.1895	63.7 hours
dmn118	BBMT	66.5299	-91.4751	47 hours
dmn119	BBMT	66.3530	-91.4702	53.5 hours
dmn120	BBMT	66.7091	-92.6427	63.1 hours
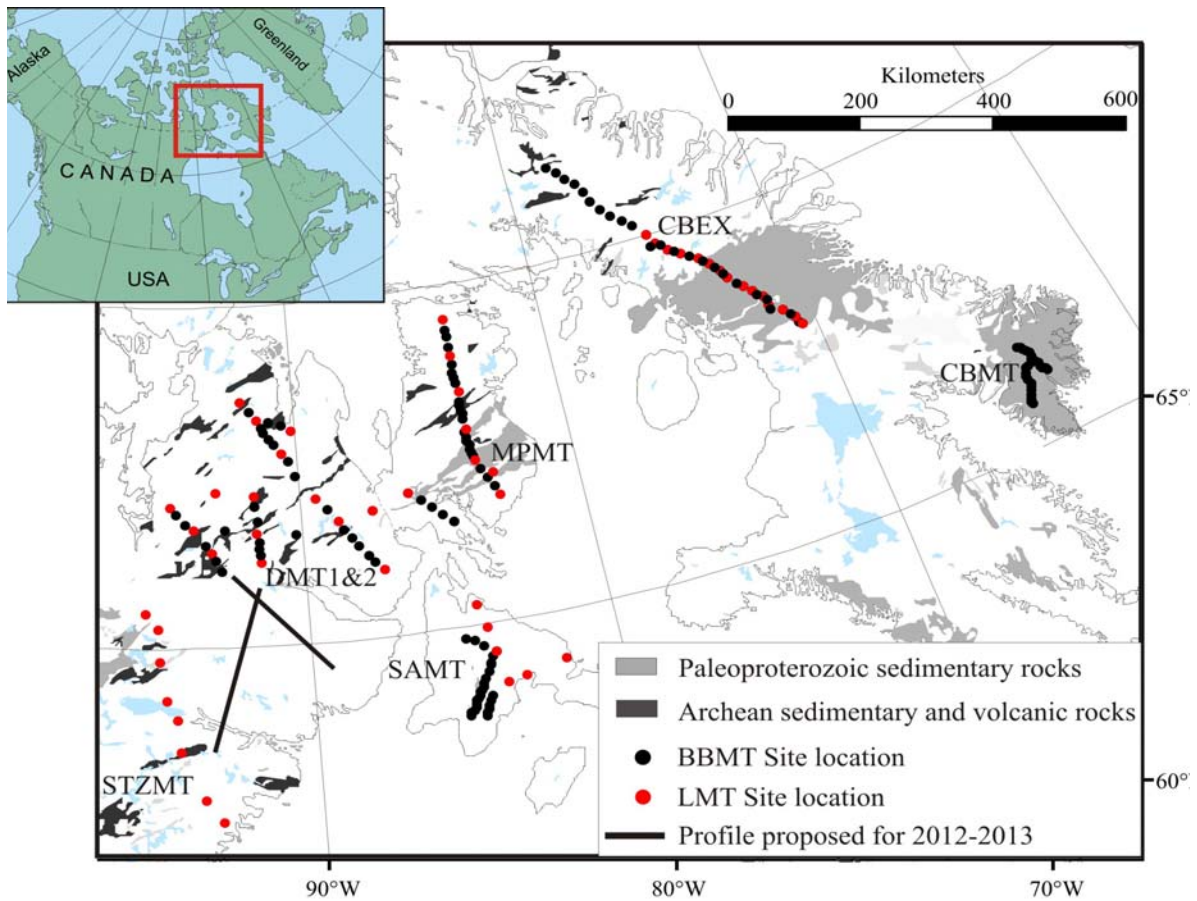
Figure 1: Regional map illustrating the locations of MT surveys in eastern Nunavut: CBEX=the Central Baffin Magnetotelluric Experiment, MPMT= Melville Peninsula Magnetotelluric survey, SAMT=Southampton Magnetotelluric survey, DMT1=Diamonds Magnetotelluric survey: 2010 data, DMT 2=Diamonds Magnetotelluric survey: 2011 data, CPMT=Cumberland Peninsula Magnetotelluric survey, and STZMT=Snowbird Tectonic Zone Magnetotelluric survey.
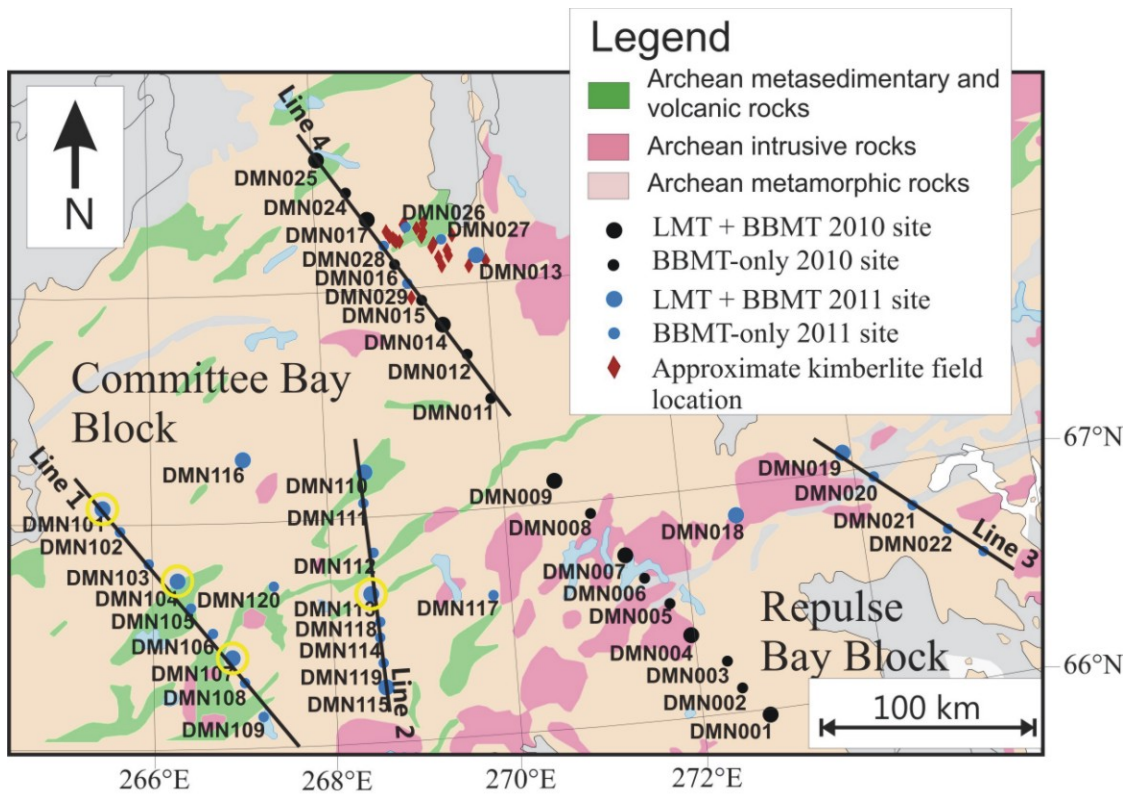
Figure 2: Geological map of the survey area showing the location of the MT sites recorded. The black lines mark the profile traces used for 2-D modelling and the yellow circles mark the location of examples of the response curves shown in figure 3.
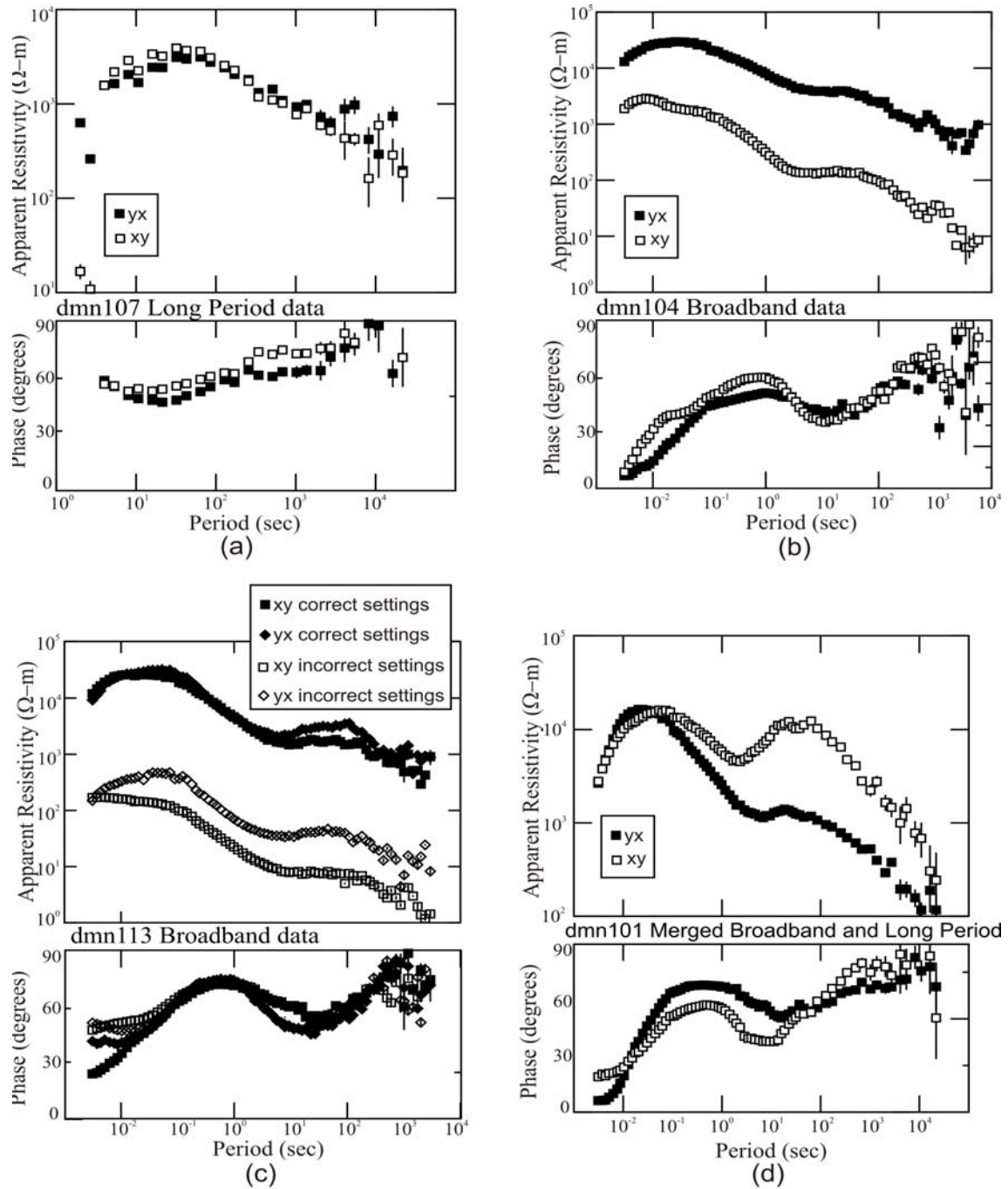
Figure 3: Examples of apparent resistivity and phase MT response curves for data measured at four sites: (a) shows an example of the long-period data recorded, (b) shows an example of the broadband data, (c) shows an example of the static shift effects of using inappropriate filter settings, and (d) shows merged broadband and long-period data at a site located within resistive Archean orthogneiss.
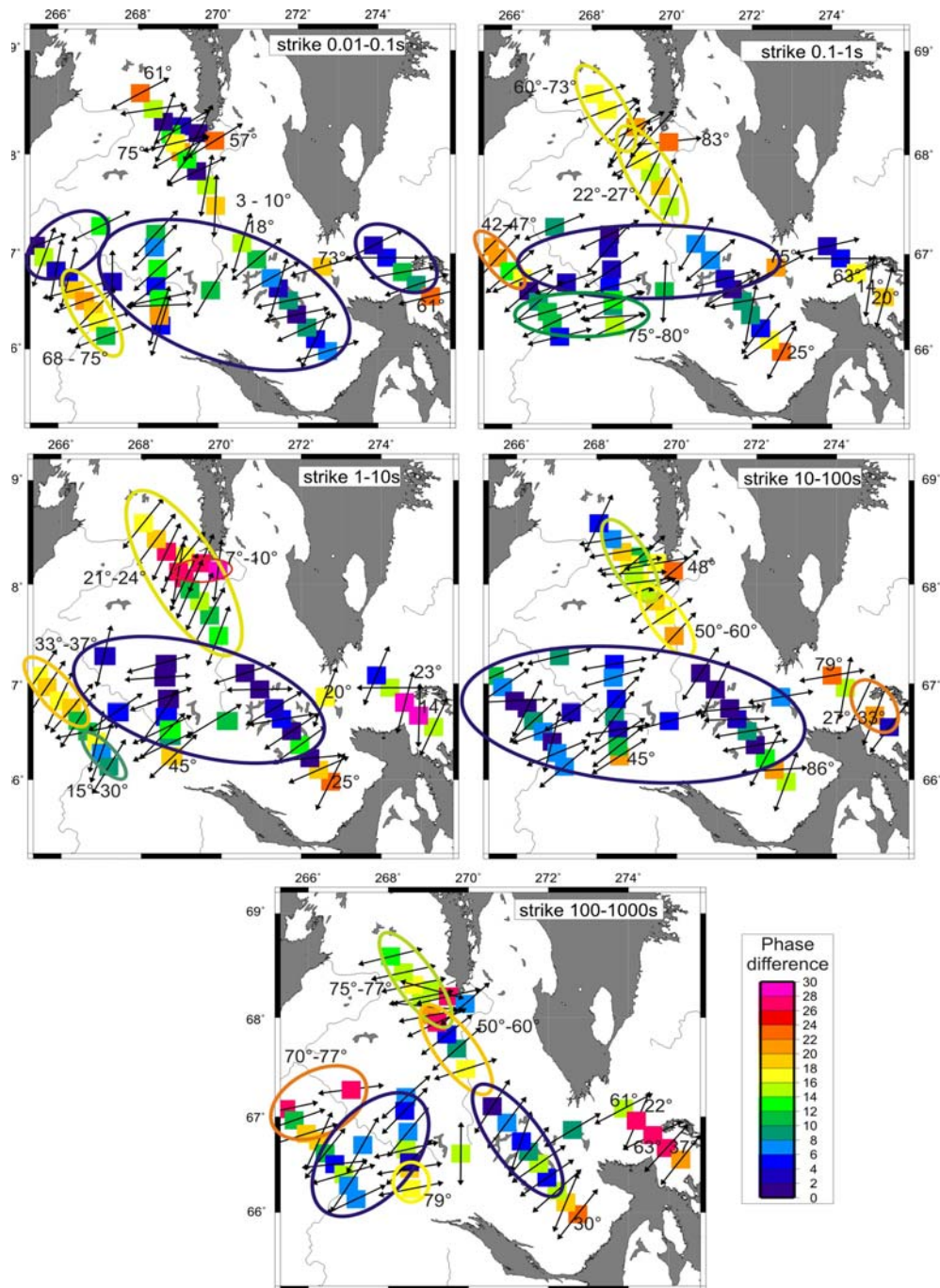
Figure 4: Maps showing the preferred geo-electric strike direction at each of the 2010 and 2011 sites for decade period bands. The color scale illustrates the maximum difference between the TM- and TE-mode phases. The blue ellipses show areas where the data can be regarded as 1-dimensional, the yellow and red ellipses illustrate the location and period range where the model will be most dependent on the geo-electric strike angle.
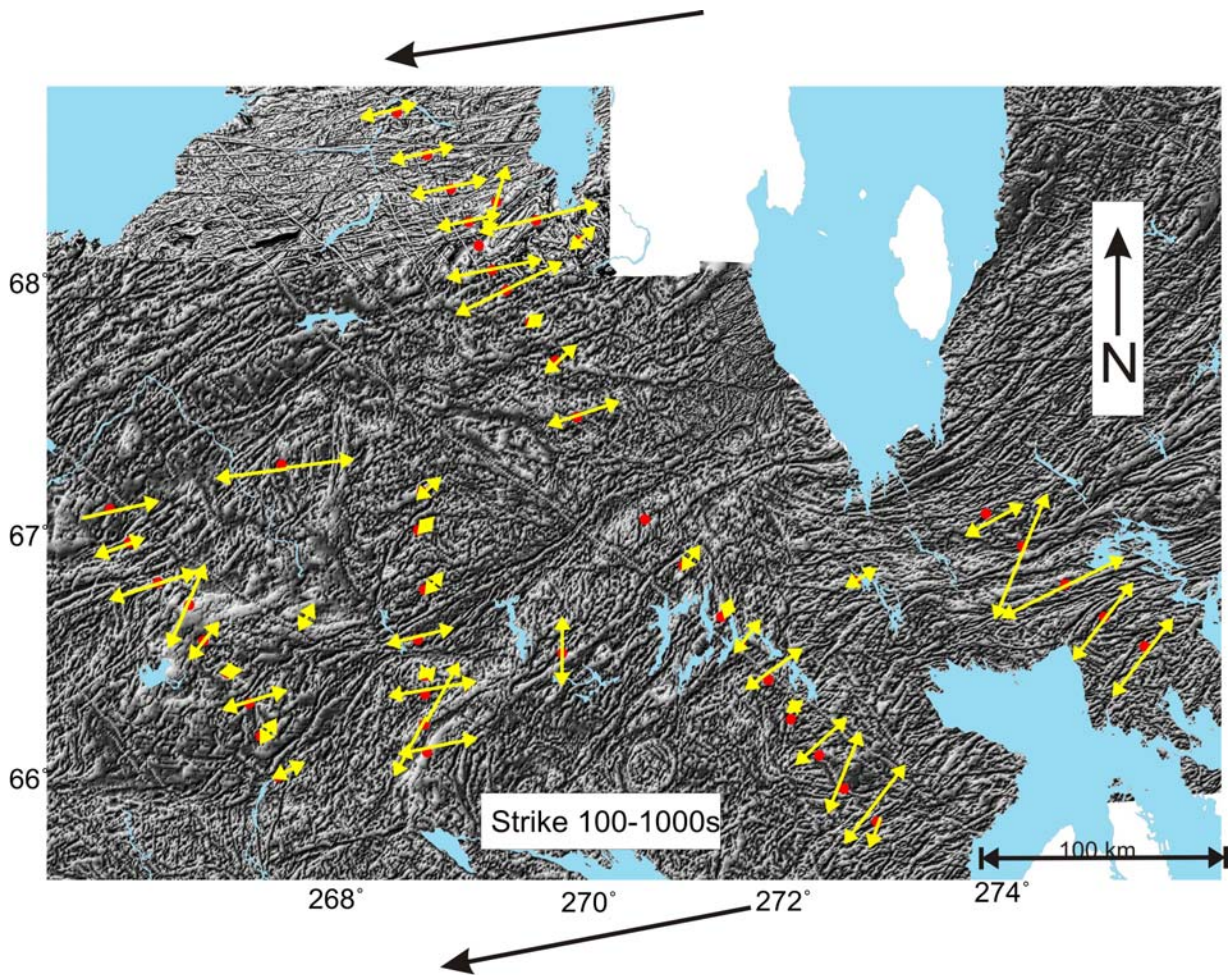
Figure 5: Map of the MT survey area showing the aeromagnetic tilt data. The yellow arrows show the preferred geo-electric strike direction at the 100–1000s period bandwidth; the length of the yellow arrows is scaled by the maximum phase difference between the TM and TE modes. The black arrows mark the direction of the North America plate motion vectors.
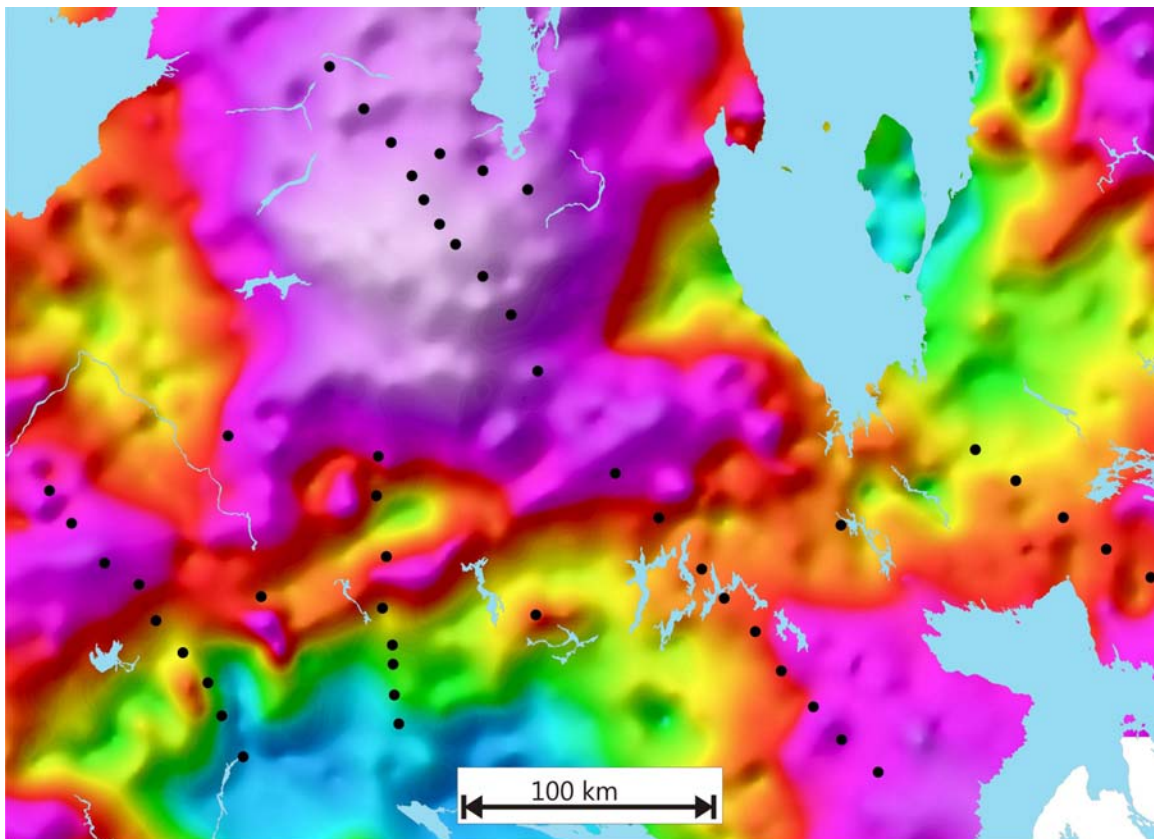
Figure 6: Map of the MT survey area showing the Bouguer gravity data.
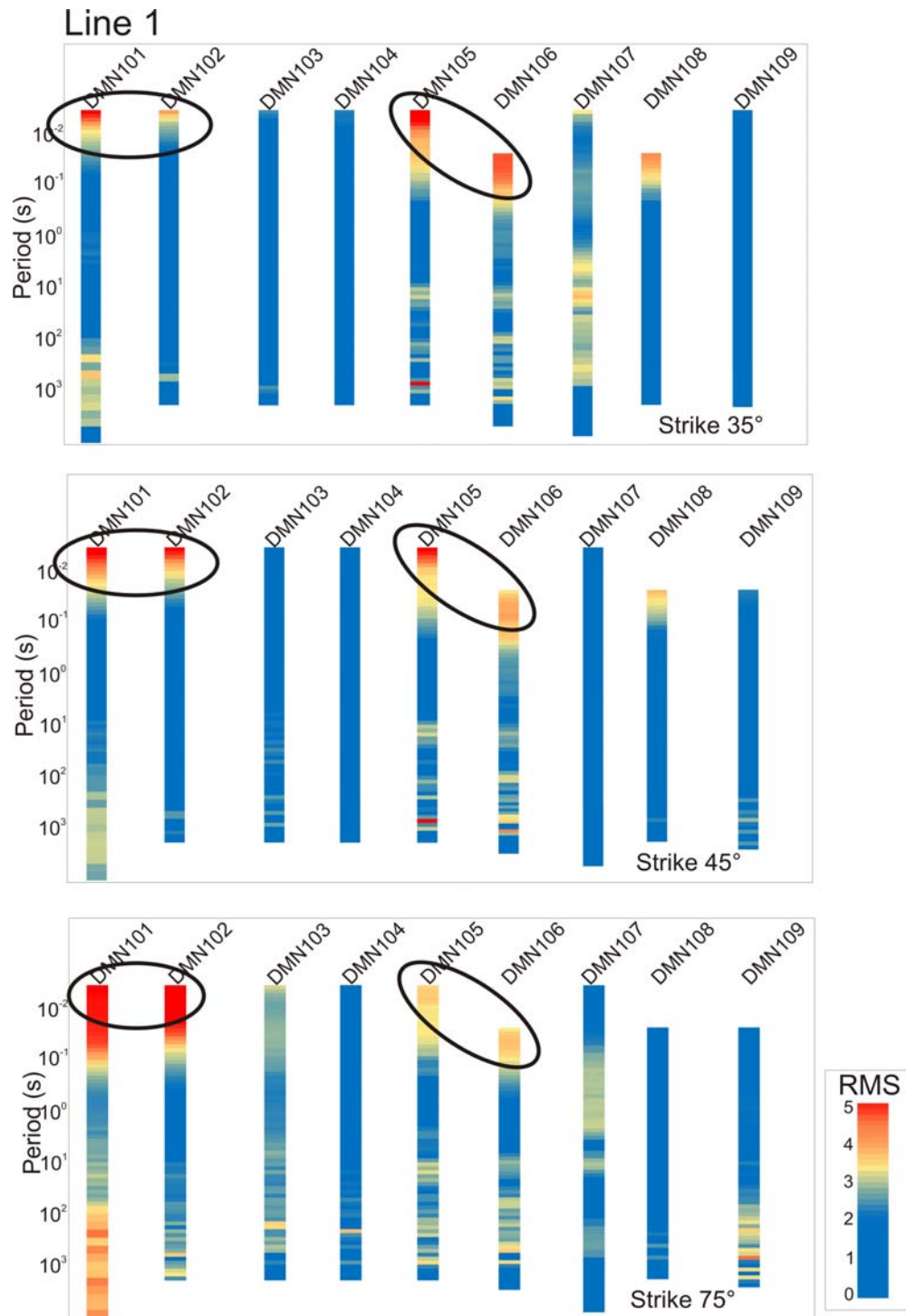
Figure 7: Data misfit values at each site over the whole recorded period range for data along line 1, recalculated at a geo-electric strike direction of 35° (a), 45° (b) and 75° (c). The black ellipses mark data that do not fit at any strike angle.
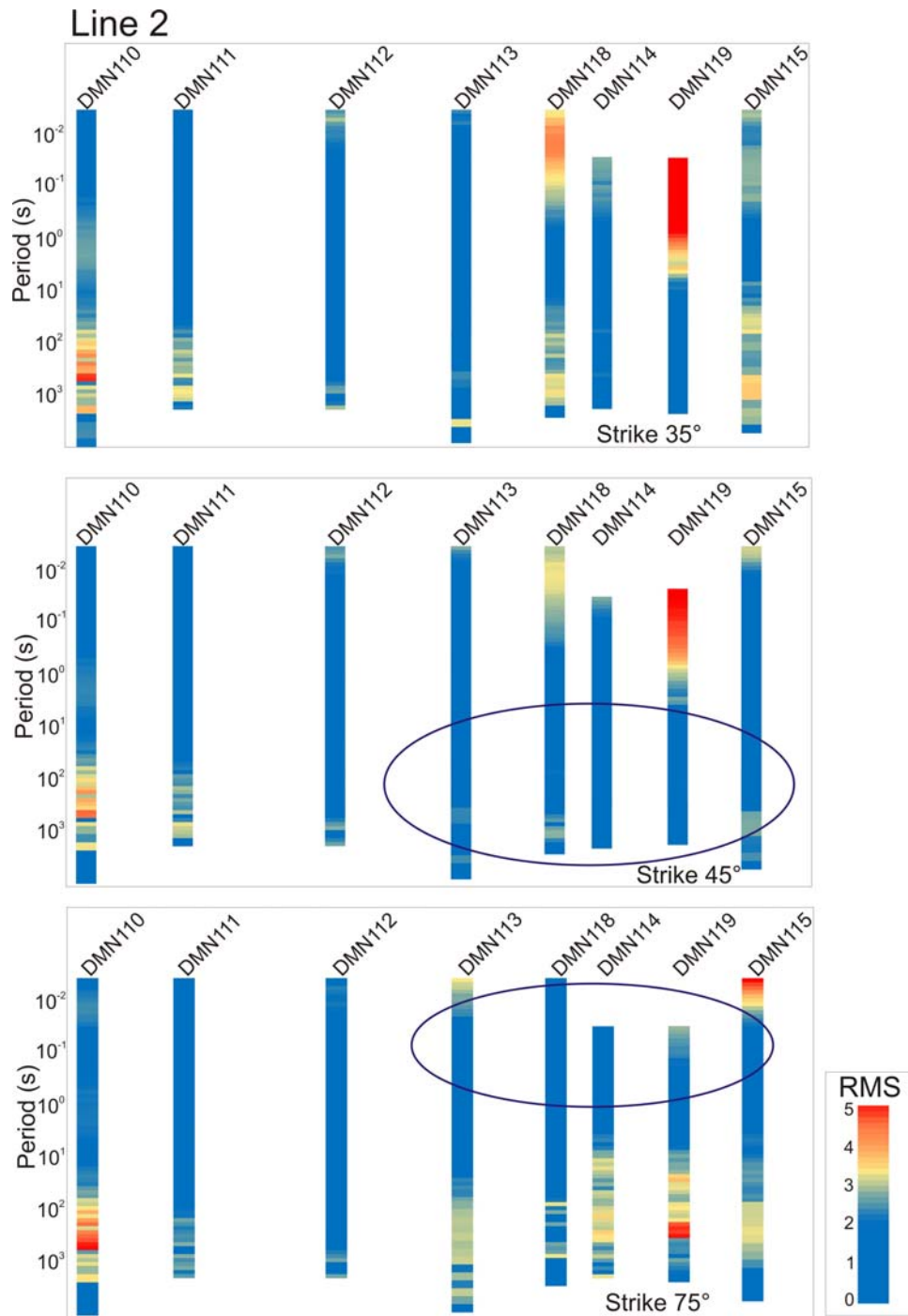
Figure 8: Data misfit values at each site over the whole recorded period range for data along line 2, recalculated at a geo-electric strike direction of 35° (a), 45° (b) and 75° (c). The blue ellipses mark data that have low RMS values at a particular strike angle.
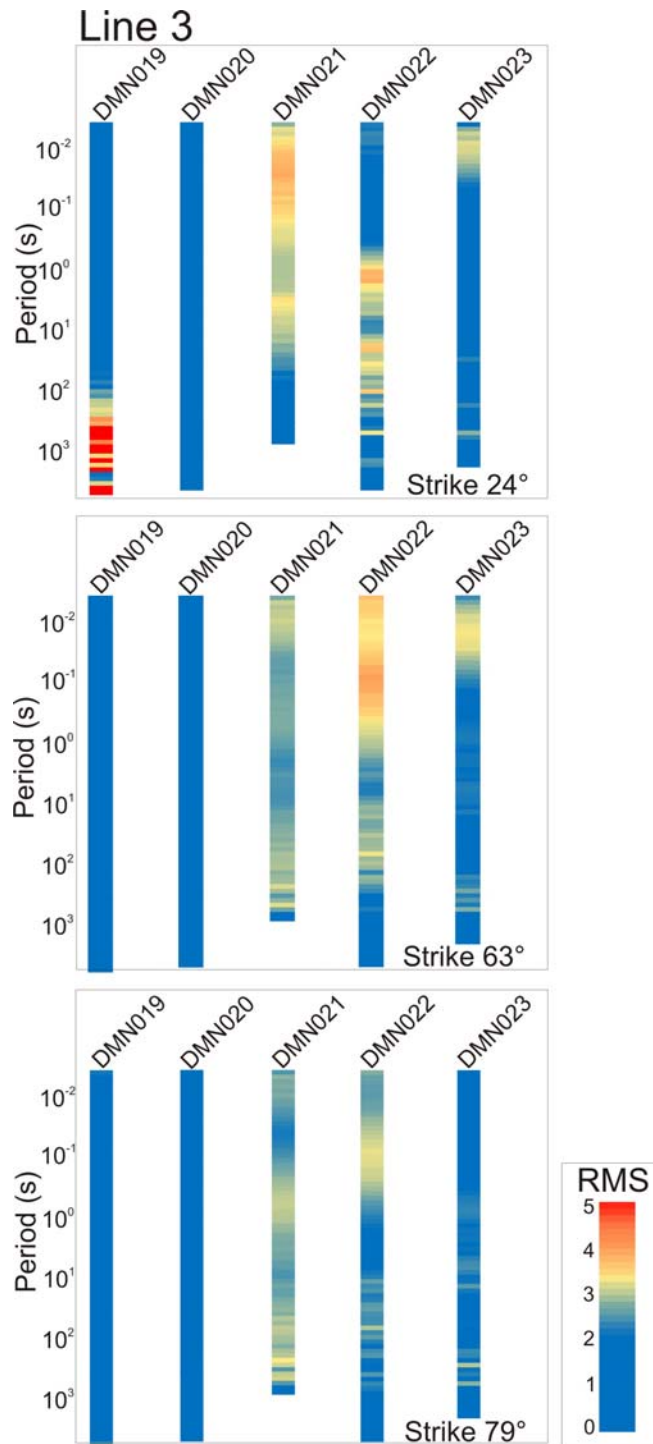
Figure 9: Data misfit values at each site over the whole recorded period range for data along line 3, recalculated at a geo-electric strike direction of 24° (a), 63° (b) and 79° (c).
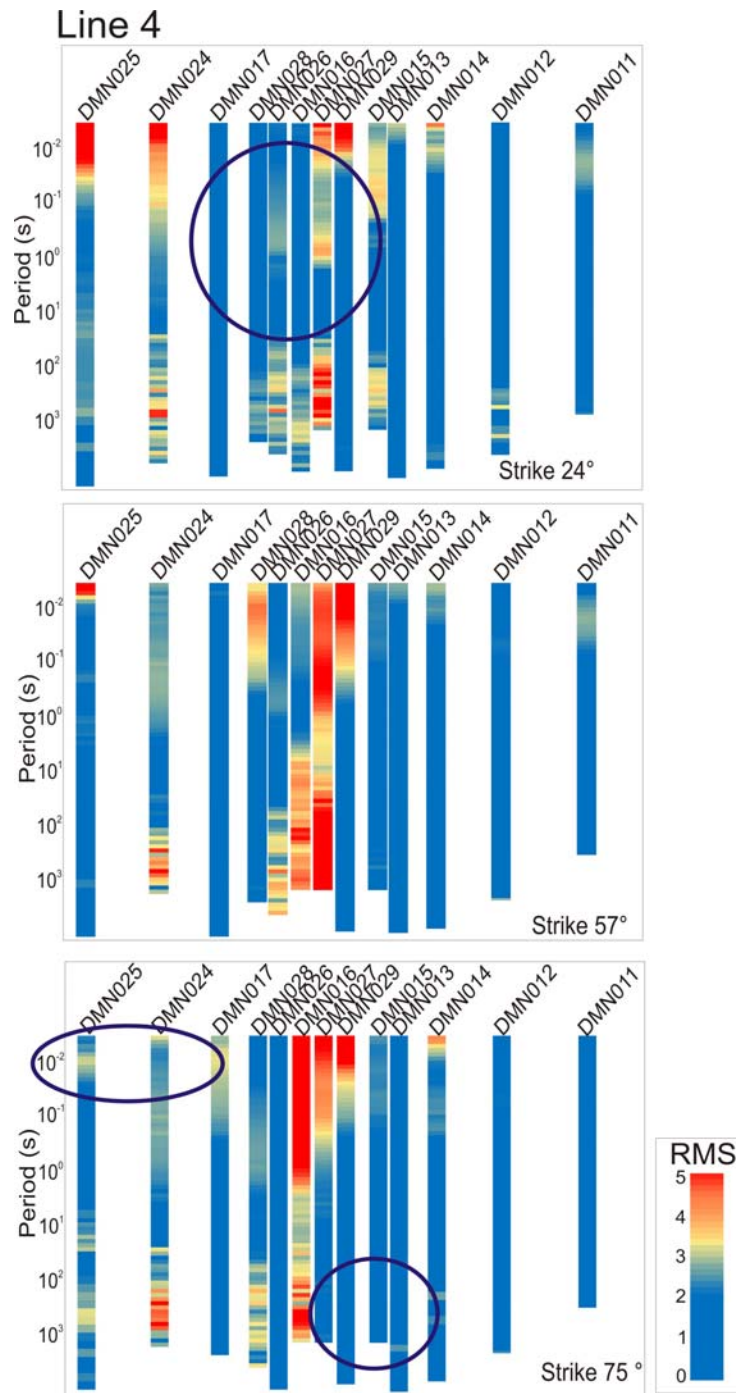
Figure 10: Data misfit values at each site over the whole recorded period range for data along line 4, recalculated at a geo-electric strike direction of 24° (a), 57° (b) and 75° (c). The blue ellipses mark data that have low RMS values at a particular strike angle.

Estimated Depths of Penetration
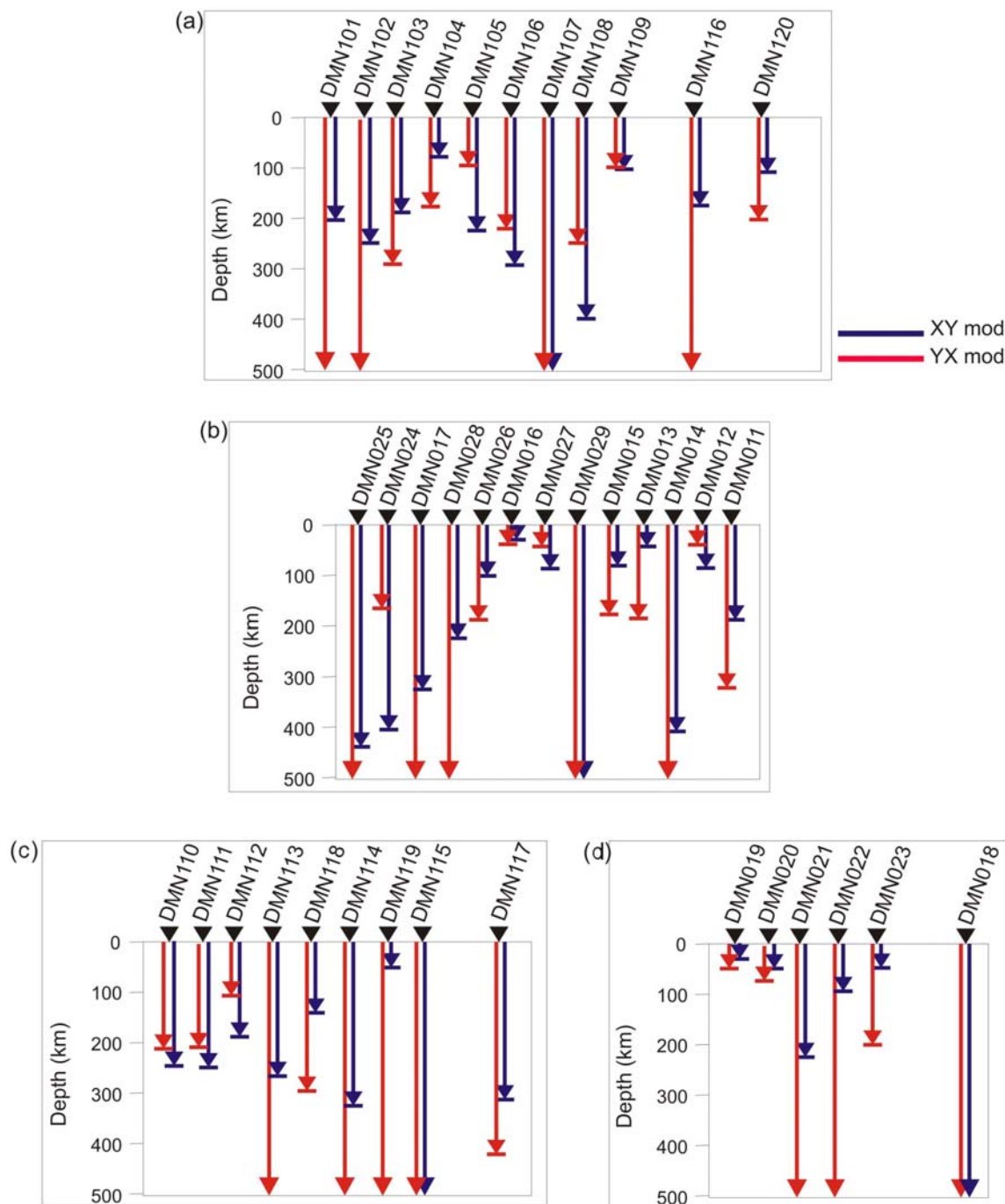
Figure 11: Estimates of maximum penetration depths for each mode beneath each MT site. (a) shows the results along line 1, (b) shows the results along line 4 including the sites acquired in 2010, (c) shows the results along line 2, and (d) along line 3.
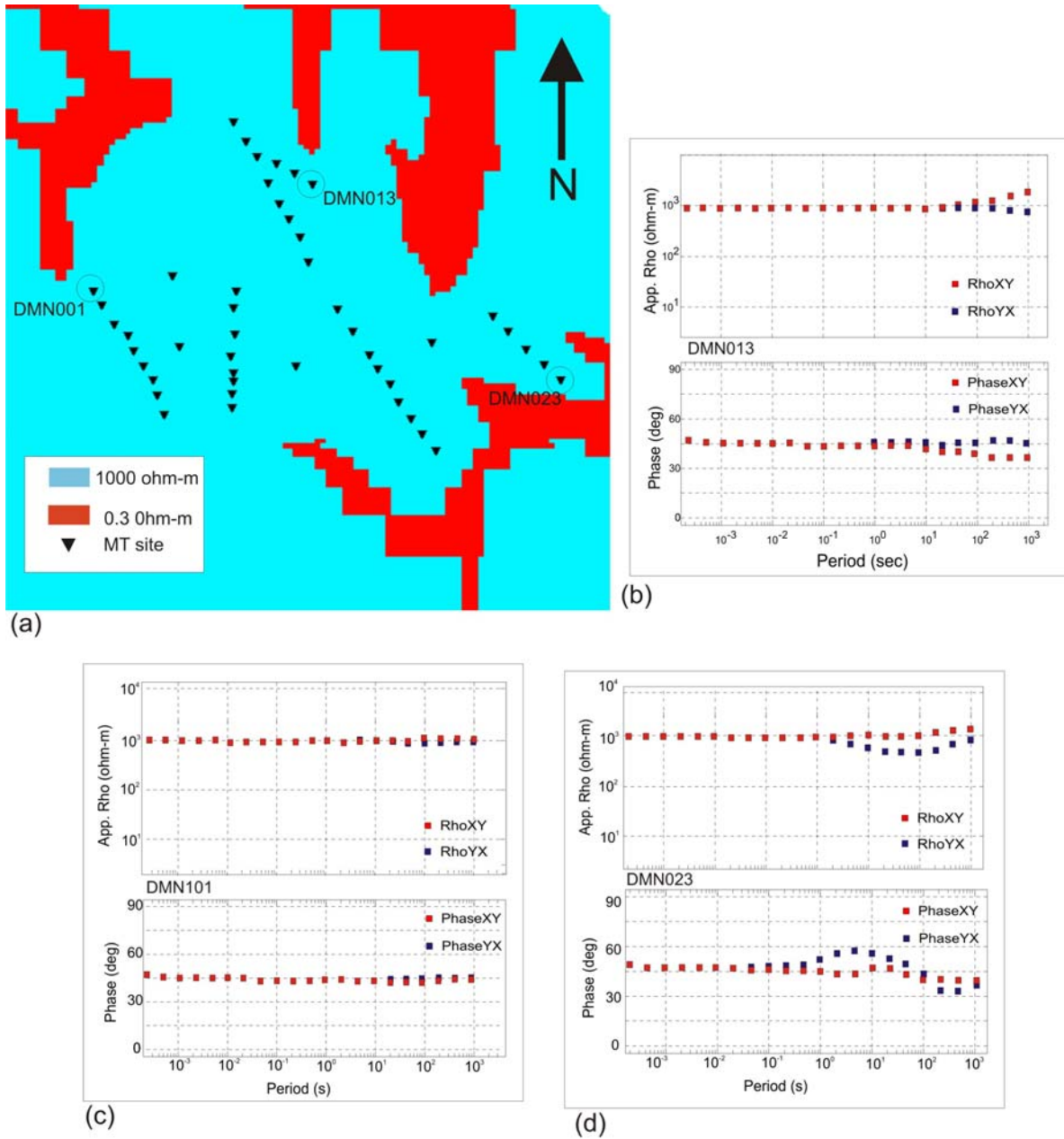
Figure 12: The 3-D mesh of the MT survey area showing the land versus ocean conductivity contrast (a). Examples of the forward calculated response curves are shown for sites DMN013 (b), DMN101 (c), and DMN023 (d).
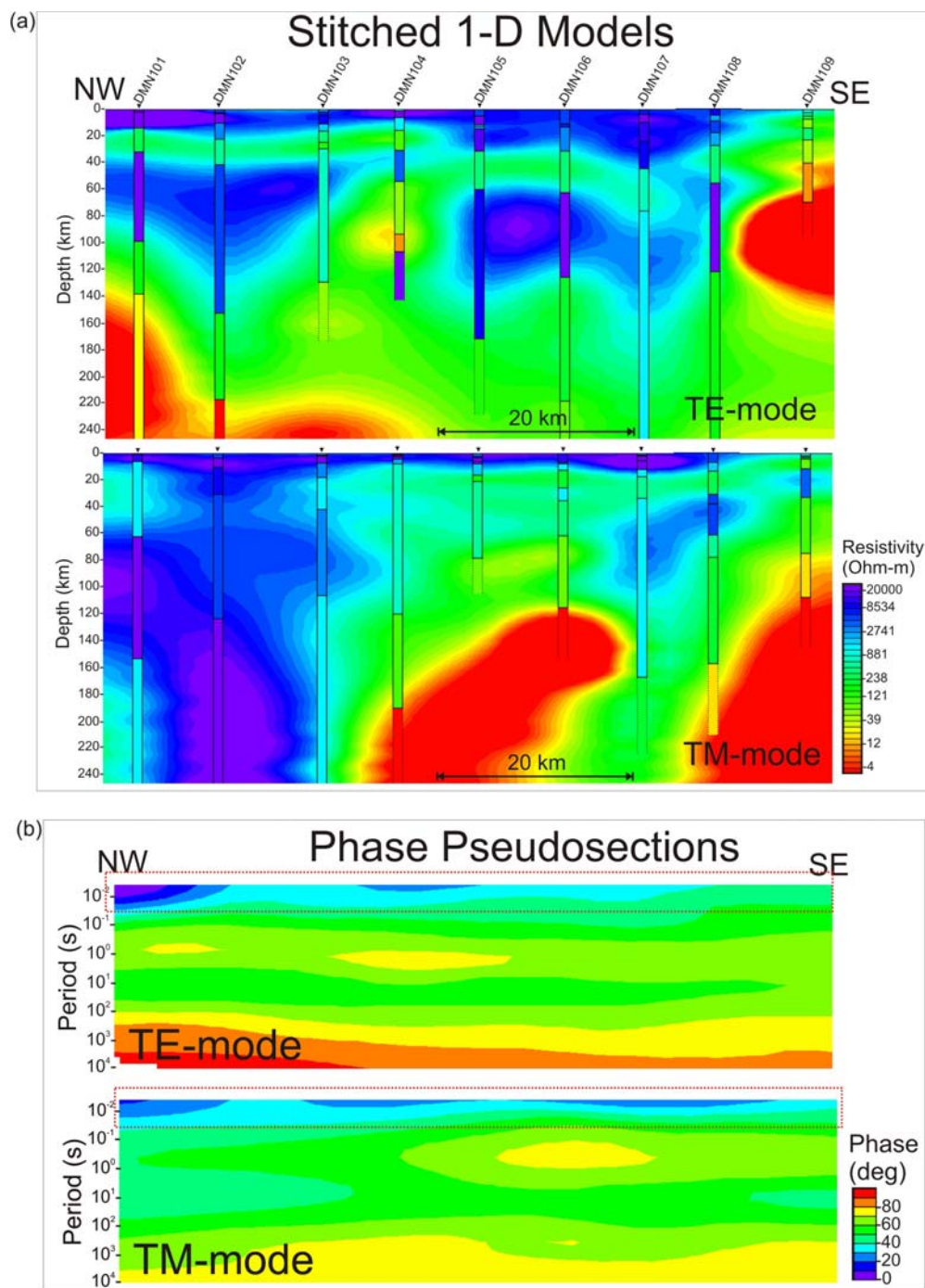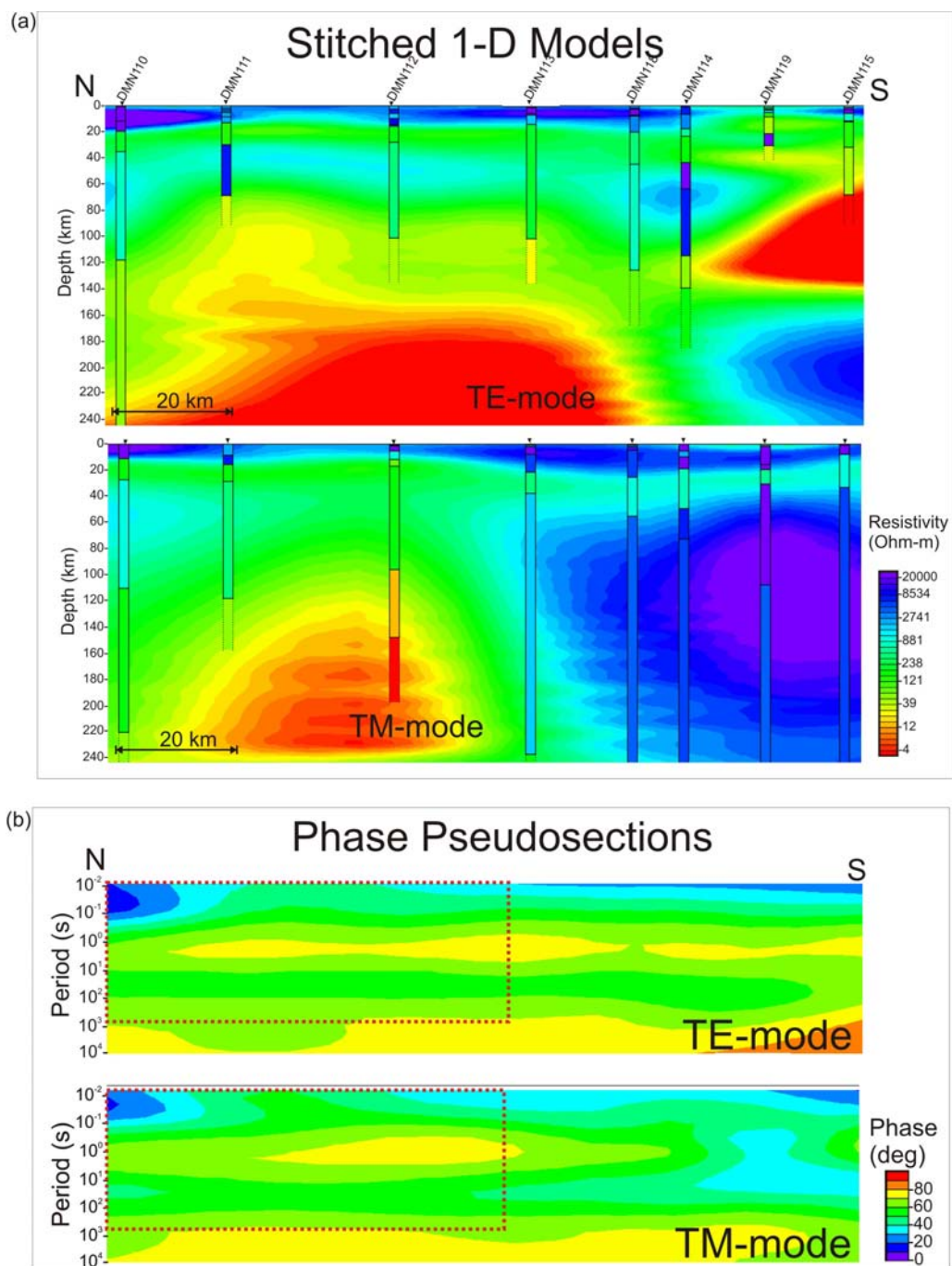
Figure 13: (a) Cross-sections along line 1, the westernmost profile illustrating the results of 1-dimensional Occam inversions in the TE- (top) and TM- (bottom) modes. (b) Pseudosections along of the phases of the sites along line 1, with increasing period of both the TE- (top) and TM- (bottom) modes. The dashed red box illustrates where the data can be considered 1-D, at periods greater than 0.08s, the data appear to be predominantly 2-D.
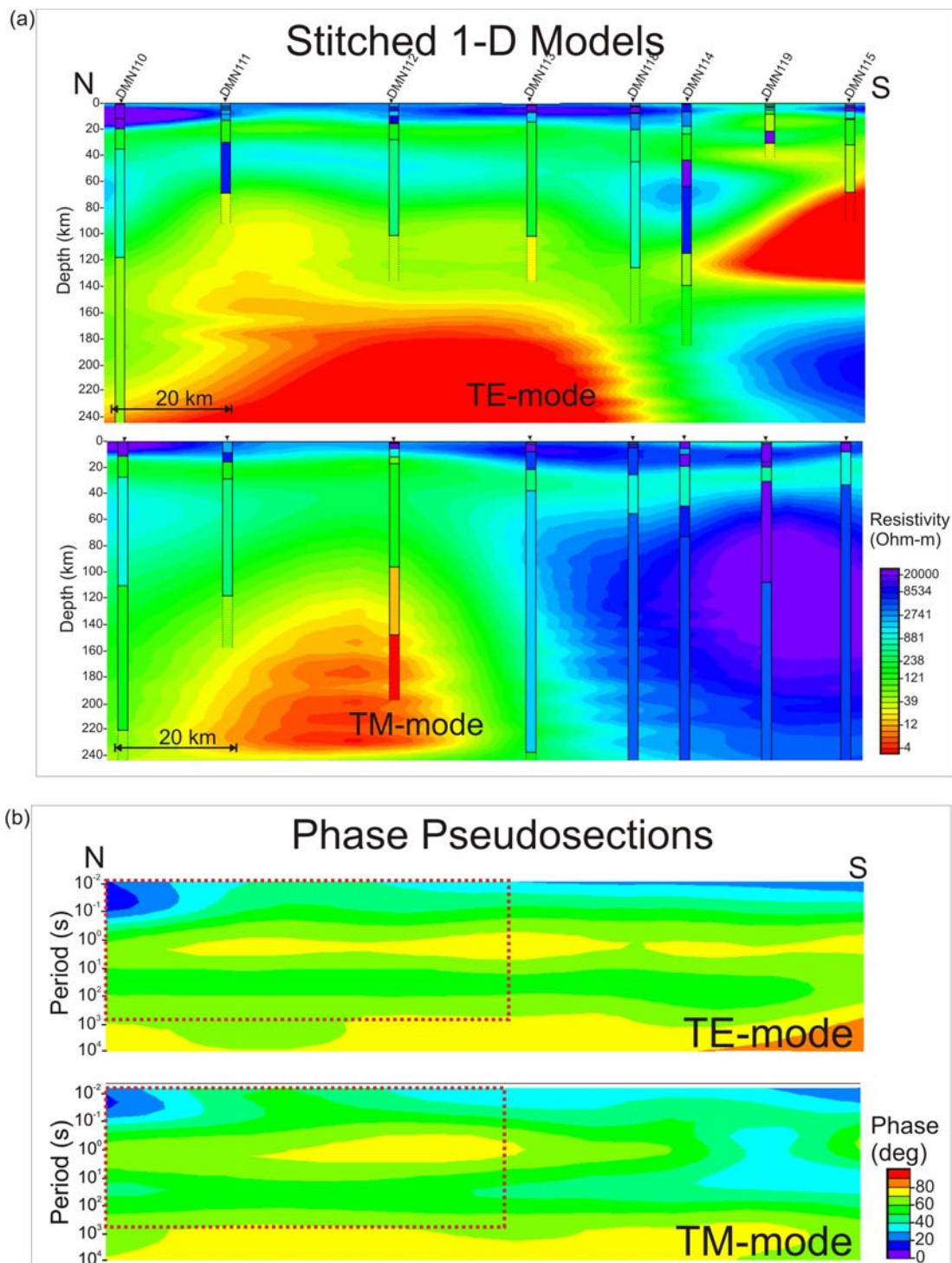
Figure 14: (a) Cross-sections along line 2 illustrating the results of 1-dimensional Occam inversions in the TE- (top) and TM- (bottom) modes. (b) Pseudosections along the western most profile of the phases of the sites along line 2, with increasing period of both the TE- (top) and TM- (bottom) modes. The dashed red box illustrates where the data can be regarded as 1-D.
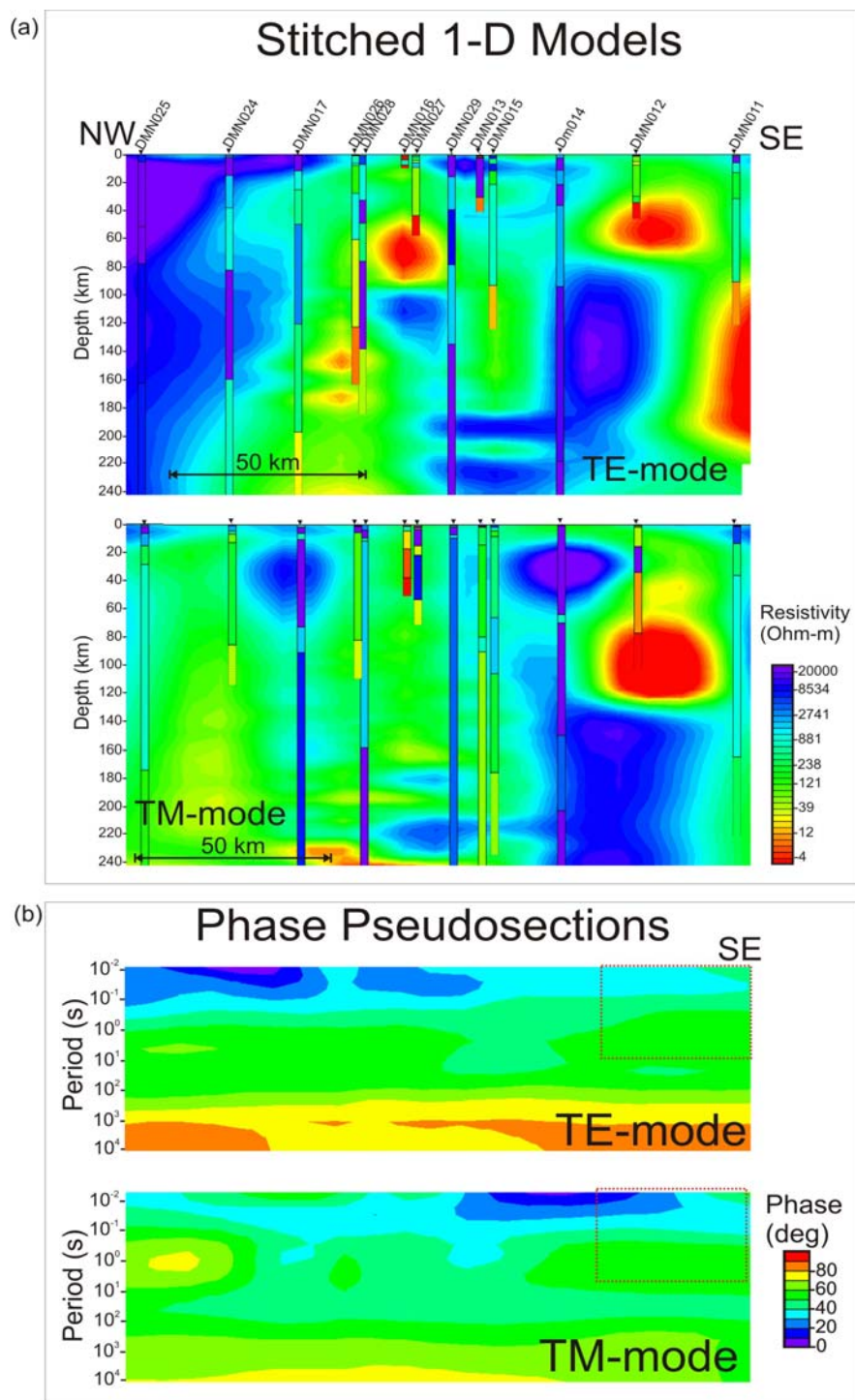
Figure 15: (a) Cross-sections along line 3, the easternmost profile, illustrating the results of 1-dimensional Occam inversions in the TE- (top) and TM- (bottom) modes. (b) Pseudosections along the western most profile of the phases of the sites along line 2, with increasing period of both the TE- (top) and TM- (bottom) modes.

Figure 16: (a) Cross-sections along line 4 illustrating the results of 1-dimensional Occam inversions in the TE- (top) and TM- (bottom) modes. (b) Pseudosections along the western most profile of the phases of the sites along line 2, with increasing period of both the TE- (top) and TM- (bottom) modes. The dashed red box illustrates where the data can be regarded as 1-D.
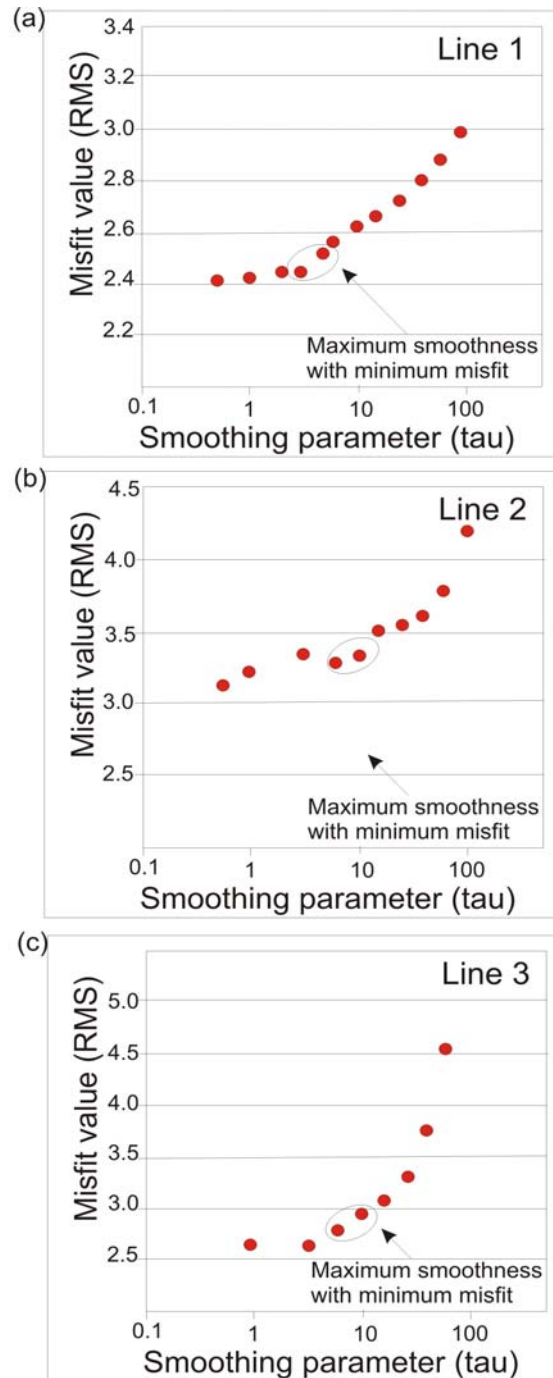
Figure 17: Plots of the trade off between the RMS misfit of the model to the data and the tau value of the inversion. (a) shows the results after 100 iterations along line 1, (b) shows the results along line 2, and (c) shows the results along line 3. The black ellipse in each plot marks the optimal tau value for each line.
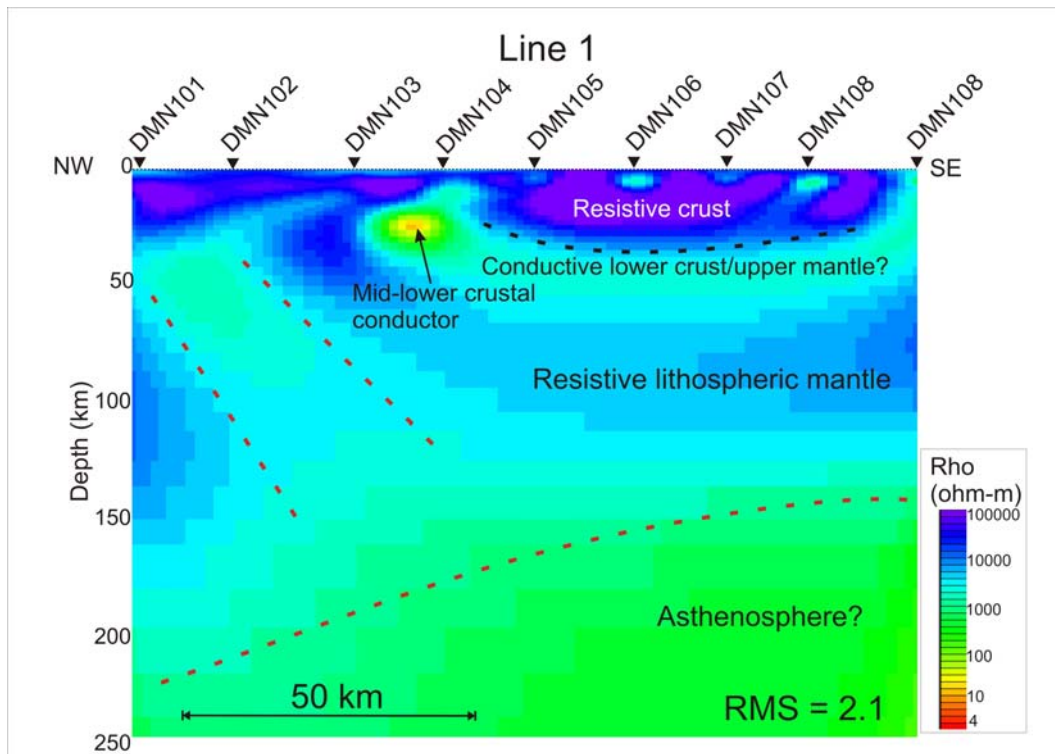
Figure 18: Preliminary model showing the conductivity structure of the lithosphere beneath line 1, the westernmost 2011 Diamonds MT profile. The red colours illustrate areas of low resistivity and the blue colours represent resistive material. The dashed red lines marks the boundary between the lithosphere and underlying asthenosphere, and illustrates structure within the mantle lithosphere. The black dashed line marks the base of the crust.
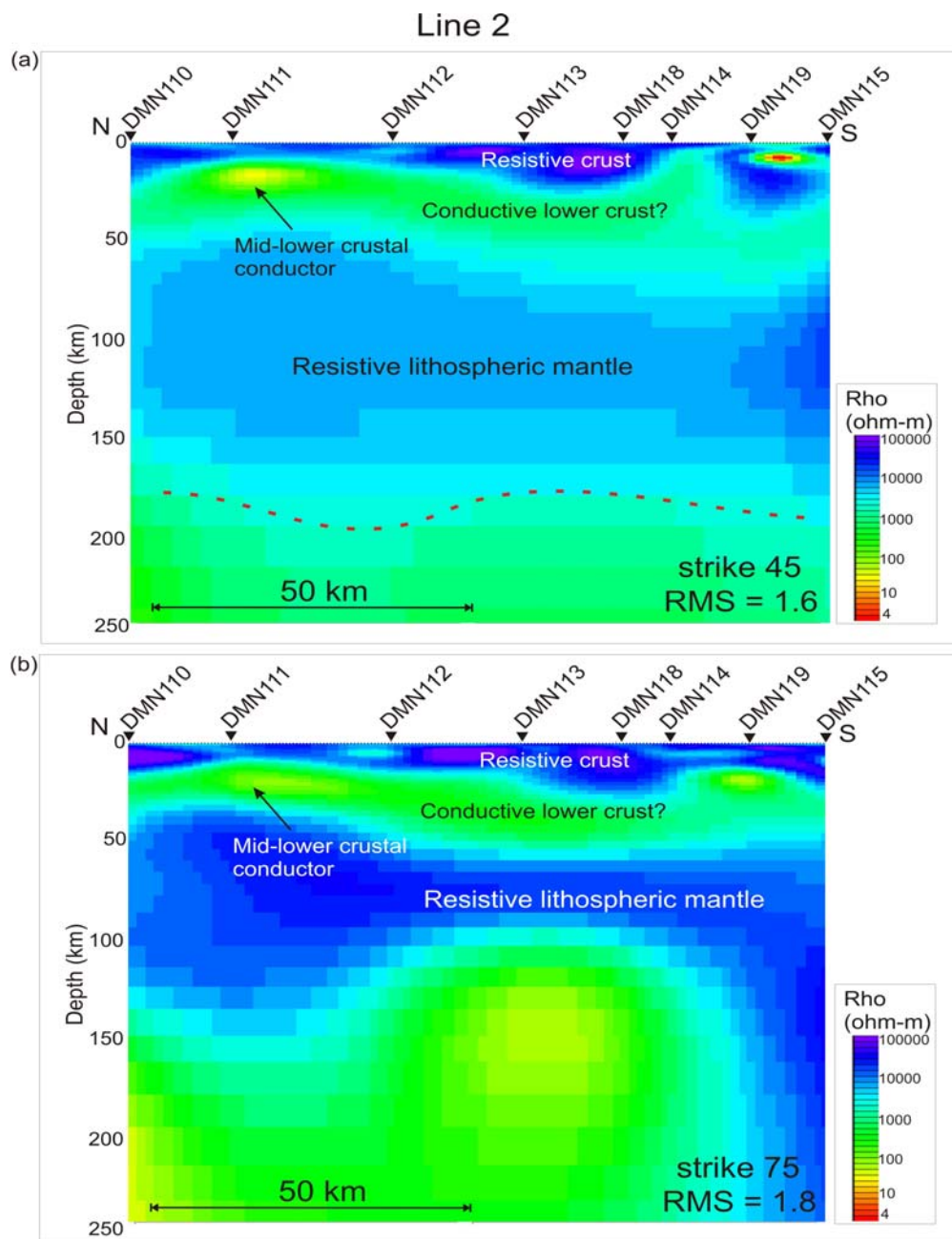
Figure 19: Preliminary models showing the conductivity structure of the lithosphere beneath line 2, (a) shows results of modelling the data at a strike angle of 45° and (b) shows the results at a strike angle of 75°. The red colours illustrate areas of low resistivity and the blue colours represent resistive material. The dashed red line marks the boundary between the lithosphere and underlying asthenosphere, and illustrates structure within the mantle lithosphere.
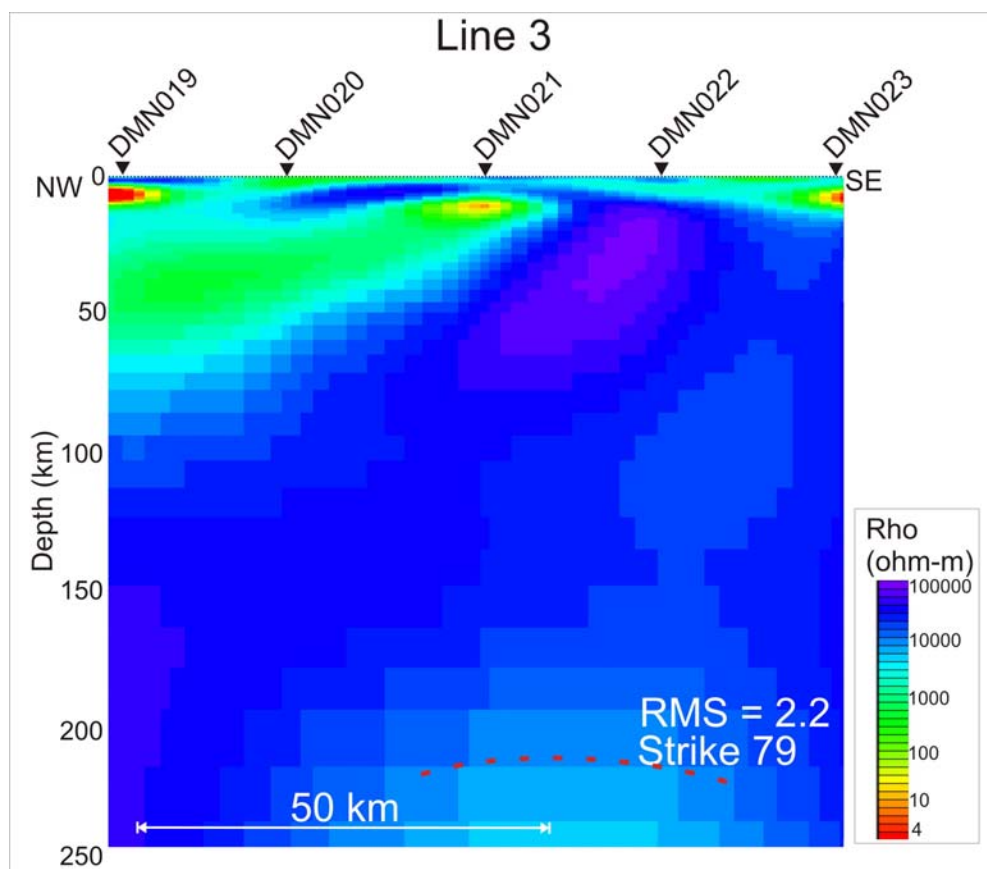
Figure 20: Preliminary model showing the conductivity structure of the lithosphere beneath line 3, the easternmost 2011 Diamonds MT profile. The red colours illustrate areas of low resistivity and the blue colours represent resistive material. The dashed red line marks the boundary between the lithosphere and underlying asthenosphere, and illustrates structure within the mantle lithosphere. The black dashed line marks a linear structure that extends from the crust through to the upper mantle.
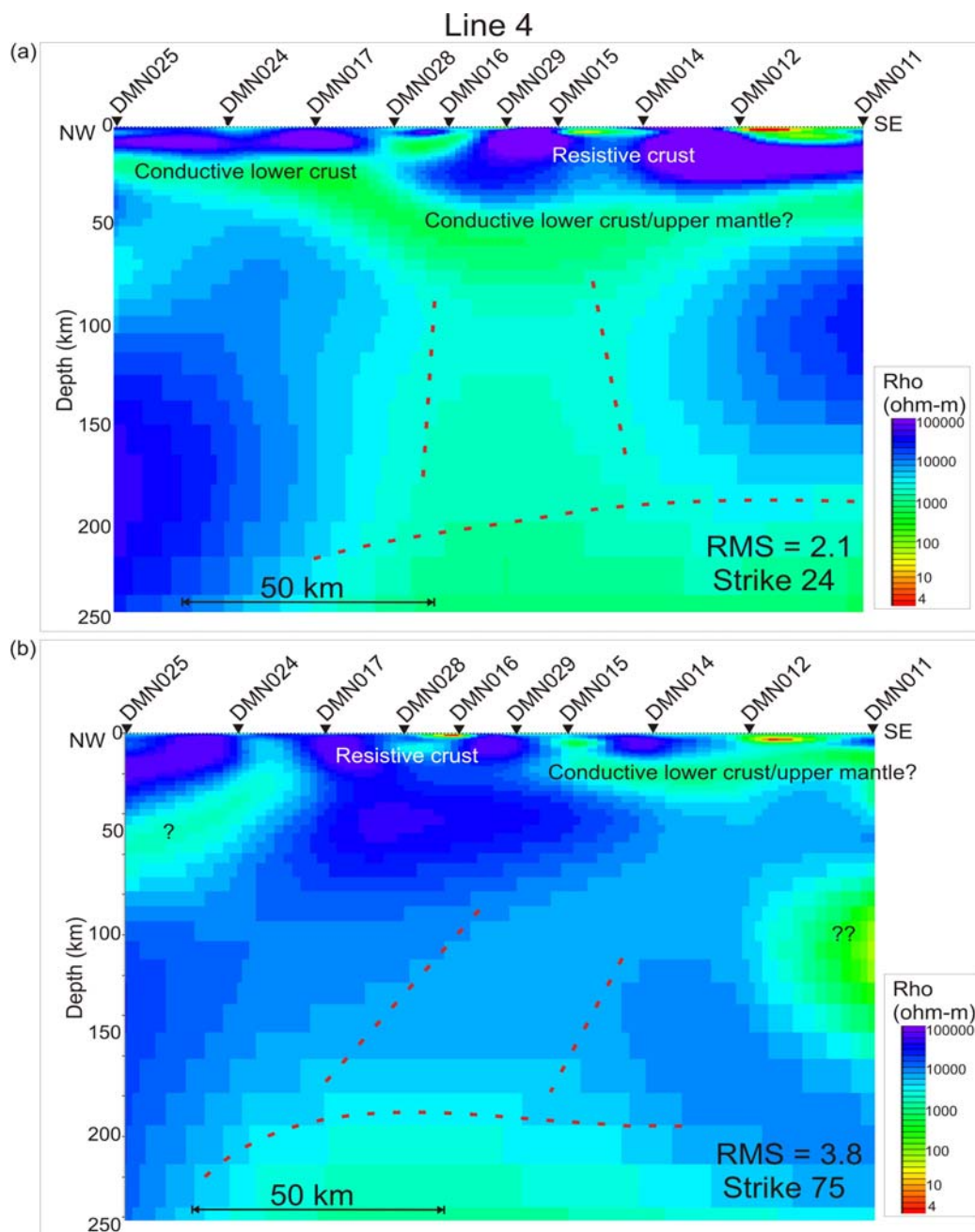
Figure 21: Preliminary models showing the conductivity structure of the lithosphere beneath line 4, (a) shows results of modelling the data at a strike angle of 24° and (b) shows the results at a strike angle of 75°. The red colours illustrate areas of low resistivity and the blue colours represent resistive material. The dashed red line marks the boundary between the lithosphere and underlying asthenosphere, and illustrates structure within the mantle lithosphere.